Aerothermal Design of an Engine/Vehicle Thermal Management System

Mitch Wolff
Air Force Research Laboratory Energy/Power/Thermal Division (AFRL/RZPE)
1950 Fifth Street
Wright-Patterson AFB, OH 45433-7251
USA

james.wolff2@wpafb.af.mil

ABSTRACT

Advances in aircraft designs through the increased electrification of various subsystems have resulted in the increased importance of thermal management. To properly design an optimized thermal management system (TMS), it is critical that the interactions between the engine and the other components be properly accounted. Before any flight begins, almost all the energy resides in the fuel, so what is done with this fuel both causes and can be utilized to help eliminate the thermal issues. The Air Force Research Laboratory Energy/Power/Thermal Division (AFRL/RZP) has implemented a research program, INVENT, to address these vital issues. The INVENT efforts have focused strongly on the development of high fidelity aircraft modeling and simulation capabilities. As a part of this initiative, AFRL has undertaken the development, integration and demonstration of a mission level tip-to-tail thermal model. The major components of the integrated model include the Air Vehicle System (AVS), the Fuel Thermal Management System, the engine models, and Power Thermal Management System (PTMS). Detailed descriptions of the importance of various drivers of the engine transient behavior are given with description of the other subsystem models. Also, information detailing compact heat exchanger designs is provided. The integrated model is then flown over a complete aircraft flight mission from ground idle thru take-off, climb, cruise, descent, landing and post-flight ground hold. Having established a baseline level of performance for the aircraft PTMS system over the full mission length, the PTMS model is then exercised to investigate some possible design space trades. The trades include varying the engine bleed air demand for an air-cycle design as well as comparing the air cycle performance to a representative vapor cycle design. The design trades are an effort to highlight the potential application of the integrated system model. The components in this system are representative of modern/future aircraft.

1.0 INTRODUCTION

Advancements in electrical, mechanical, and structural design onboard modern more electric aircraft (MEA) have added significant stress to the thermal management systems (TMS). Traditionally, the aircraft vehicle, propulsion, and power systems have been designed and optimized at a federated subsystem level with little consideration toward the design of the TMS. Such a design philosophy was sufficient due to the low thermal resistance of the airframe skin, the addition of ram inlet heat exchangers, and the relatively small amount of power required by the electrical loads. Aircraft with composite skins have a high thermal resistance thereby greatly reducing convective cooling. In addition, the cross-sectional areas of ram inlet heat exchangers have also been reduced. At the same time, the size of the power system has increased by nearly an order of magnitude to support numerous high-power loads that increase the internal heat generated within modern/future aircraft. These factors have led to the current thermal challenges facing modern aircraft.

The power and thermal management system (PTMS) developed for modern aircraft is an integral approach combining the functions of the auxiliary power unit (APU), emergency power unit (EPU), environmental control system (ECS), and thermal management system (TMS). The combination of the functions of previously federated subsystems into an integrated system is a significant improvement by reducing weight, volume, and cost while improving reliability. This next generation PTMS has advanced system integration by combining the functions of the APU, EPU, ECS and TMS. It is more efficient because the integrated system approach allows the same turbomachinery to be used for producing power and cooling. For aircraft using federated subsystems, the APU is used only on the ground and becomes a weight penalty once airborne. The EPU is used only when the main power generation system fails. Therefore, the aircraft is penalized by the weight of the idle EPU during normal operation. In the PTMS, since the turbomachinery is used for producing power for the APU and EPU, and for producing cooling for the ECS and supporting TMS functions, the aircraft does not incur penalties. This benefit reduces weight, volume, and cost while increasing the reliability of the aircraft.

The MEA initiative imposes a new environment where the main engine operates more efficiently and electrical actuation replaces the heavy and unreliable hydraulic and pneumatic components. The introduction of the PTMS is a big step toward MEA. Future generation PTMS is expected to progress even further in this direction by more integration with the main engine, main power generation, flight control actuation, and other systems. Improved power extraction, electrical utilization, and thermal management will be achieved. Central to this whole integrated PTMS scheme is the primary propulsion system – i.e. the jet engine. The engine provides two fundamental functions in this process: 1.) bleed compressor air is used to drive the PTMS power turbine and 2.) a fan duct heat exchanger is used as the primary location of dumping waste heat. Therefore, the overall integrated vehicle engine/PTMS will be an integral part of future aircraft energy management, resulting in improved vehicle performance.

1.1 Background Overview

Future thermal management systems must be capable of operating in an on-demand mode in a highly dynamic environment. This requirement is driven by the transient boundary conditions and the high-power, dynamic, and inefficient loads that need cooling. The traditional thermodynamics approach to developing thermal management systems has been to use classical thermodynamic assumptions and overdesign the thermal management system for peak (anticipated worst case) steady-state heat loads. This approach has been satisfactory for traditional aircraft designs, but as thermal constraints are met or exceeded as a result of increased aircraft capabilities, a more accurate method of predicting the worst case operating points has become essential.

On the other end of the spectrum, significant research is being conducted to predict performance of advanced heat exchanger designs, thermal energy storage devices, and advanced airframe materials. These conceptual designs are developed at a level of detail incapable of being evaluated over the hours that typical missions are run. Although optimized at a component level, the impacts to the system level design are difficult to predict

An intermediary approach is a transient solution capturing the dynamics of an entire mission while remaining computationally feasible. To this end, a Simulink based, system of models has been developed that can be used to predict the worst case operating conditions over multiple mission scenarios, day types, locations, while also offering the user the capability of integrating lumped parameter reductions of highly detailed conceptual designs for evaluation of TMS impacts. This integrated system of subsystems modelling and simulation (model based design) preliminary design approach is essential for developing future aircraft systems which will provide the capabilities being demanded by aviation consumers.

2.0 FORMULATION OF TMS COMPONENT MODELS

The model integration effort employs the commercial Matlab/Simulink software package as a top level modeling environment. Many of the subsystem models are developed entirely within the Simulink environment. Simulink offers a wide range of numerical integration solvers well suited for TMS heat transfer problems. As a graphical programming environment, Simulink allows for a model development that can have the look of traditional flow schematics. This allows end-users to translate from a schematic layout to a Simulink model with relative ease. The following components and sub-systems are simulated:

- Aircraft 6-DoF and vehicle management system - AVS
- Aircraft fuel thermal management system (tanks, etc.) - FTMS
- Engine performance (thrust, fuel burn rate, etc.)
- Engine fuel thermal management system (fuel pumps, etc.) - Engine
- Power thermal management system (PTMS – power turbine, heat exchangers, etc.)

A schematic of the model interconnectivity is given in Figure 1, followed by descriptions of the individual component and sub-system models.

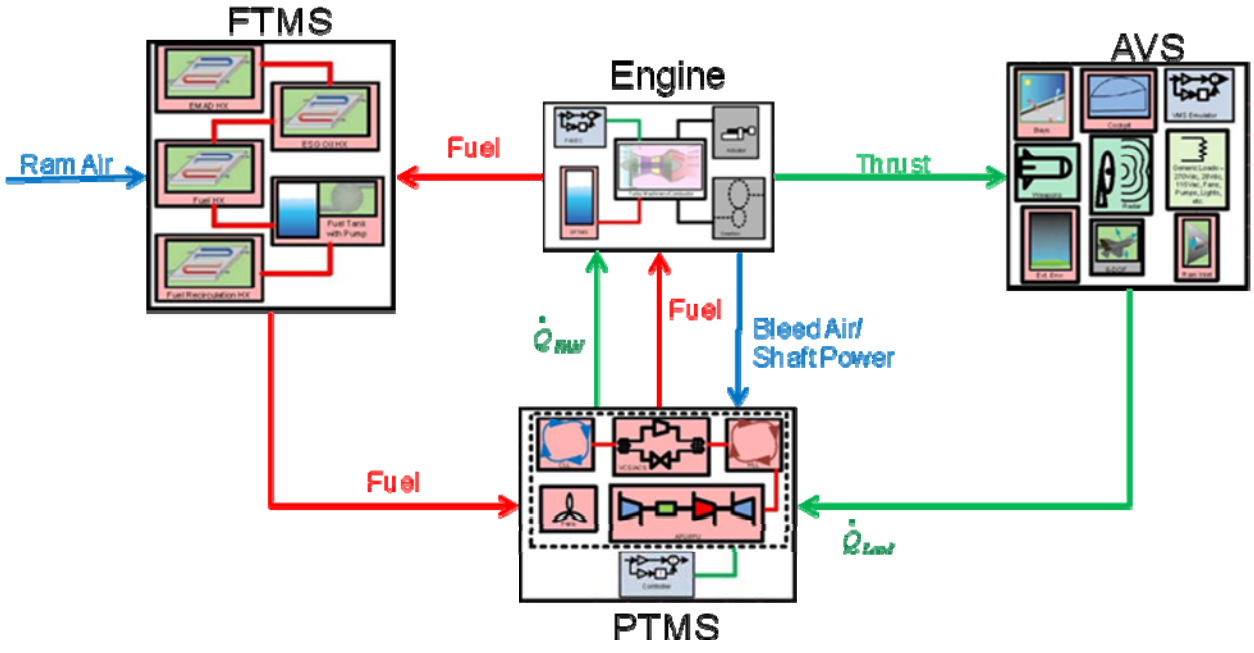

Figure 1: Top level schematic: integrated thermal model.

The various TMS components will now be discussed in detail. The level of physical modeling is dependent on the amount of uncertainty required, the funding resources and how quickly an analysis is needed.

2.1 Air Vehicle System Model

The aircraft six degree of freedom model is a variable mass, rigid body model representative of an advanced aircraft. The aircraft 6-DoF model is intended to serve as a mission level analysis tool with sufficient fidelity to enable relevant trade studies (e.g., accounting for additional ram air drag associated with a vapor cycle PTMS as compared to an air cycle PTMS) and yet with sufficient execution speed that full length mission performance metrics can be produced rapidly. The primary modeling objective for the 6-DoF model is to dynamically update the following data as a function of the aircraft flight condition: ambient atmospheric data, required engine thrust, and a coordinated set of control surface actuator loads. The model that has been developed for the present air platform is a MATLAB/Simulink application with the following features and capabilities:

- Trim and IC capability for steady level flight at any point within the flight envelope.
- Easily specified mission legs in terms of altitude, Mach number, roll angle and course.
- Aircraft weight, inertia tensor and cg location dynamically updated throughout the mission.
- Control effectors: wing-tip "clamshells" for directional and braking control; outboard elevons for roll control; beavertail and inboard elevons for pitch control.
- Symmetrical engine thrust – no differential thrust control, no thrust vectoring.
- Vehicle aerodynamics based on table look-up scheme; aerodynamic database developed using a vortex-lattice method.
- In standalone mode, inclusion of a dynamic engine thrust model.
- Ability to integrate instantaneous data over the length of the mission to arrive at performance metrics such as range, endurance, total fuel burn, etc.
- Flight control loop closure providing cruise regulation and tracking of altitude, airspeed or Mach number, bank angle and heading.
- Feedback gains scheduled throughout the flight envelope as a function of gross weight and freestream dynamic pressure.

2.2 Transient Engine Model

A thermal and an aerodynamic model of the engine are used to simulate engine behavior. The aerodynamic model simulates the temperature, speeds, pressures, and thrust of the engine cycle. The thermal engine model simulates the heat transfer of the various components of the engine to the fuel. The thermal model has inputs from the aerodynamic model of temperatures, speeds, pressures, fuel flow, and power extractions. The outputs from the thermal model include temperatures of the oil and fuel and a return to tank flow. The inputs to the aerodynamic engine model include thrust commands, ambient conditions, power extraction, bleed requests, and heat inputs. The power extractions from the engine are estimates of electrical loads throughout the flight envelope. The bleed request and heat input into the engine air stream are signals from the PTMS system. The thrust command is generated by the aircraft 6-DoF model. Outputs of the aerodynamic engine model include fuel burned, thrust achieved, and inputs to the thermal engine model mentioned above.

2.2.1 Background

Numerical Propulsion System Simulation (NPSS) provides a flexible framework capable of handling the complex coupled equations that define engine cycles as well as other systems[1,2,3]. It can handle linear and non-

linear differential equations and has several solvers available. The entire system is laid out where each mechanical, electrical, hydraulic, etc. component is represented by one or more Elements. Within each Element, Subelements and Sockets can be used to provide hierarchy for the details. Each engine component can be represented as a 0-dimensional lumped unit, as a full 3-dimentional unit, or anything in between. There can even be a mixture of component fidelities represented within a model, provided that the appropriate mapping is created to "zoom" between high- and low-fidelity components at their interfaces.[4]

An NPSS engine model of a double bypass, mixed flow turbofan architecture was developed in previous work[1]. The primary focus of that work was the optimization of the variable geometry features of the engine to complete missions that would not be achievable with traditional engine architectures. Overall, this model is representative of a modern implementation of a varable cycle engine (VCE), but represents no specific engine or platform. The data used in the model is considered "reasonable" and assumes some technology advances in material properties, component efficiencies, etc.[5]

While included in the model layout, the afterburner is not used in this current research effort (i.e. its fuel flow rate remains zero). All components in this model are lumped 0-dimensional elements, though sockets and subelements are utilized to add fidelity to each component without adding spatial dimensions. Because this model was originally used for preliminary design and sizing, it was a steady-state cycle balance model in which no transient behaviors were captured. Missions were simulated as a handful of steady-state design- or off-design points that were maintained for a mission segment of a specified time duration.

2.2.2 Dynamic Engine Modeling

The current TMS effort required the addition of the time dimension to the previous model. This was accomplished by adding time transient effects to the existing model. The NPSS framework has numerical integration routines (both explicit and implicit methods are available) built into its solver. Some standard Elements are coded to capture transient effects if run in that mode; other effects were more challenging to include.

The first of these transient effects added is simple inertial shaft dynamics. This involves a torque (or power) imbalance on the shaft that results in acceleration or deceleration. This contrasts with the traditional approach of the cycle deck model which instead performs a shaft balance (i.e. net torque or power is zero) at the design or off-design point of interest. In this context, "shaft dynamics" refers to the inertial effect of the shaft itself and the attached turbomachinery, not the torsional effect of shaft wind-up. It is modeled as[1]

$$\frac{dN}{dt} = \frac{T_q}{J_{sum}} \frac{60}{2\pi} \tag{1}$$

where N is the shaft speed (in revolutions per minute, RPM, by using the $\frac{60}{2\pi}$ factor), t is time, T_q is the net torque on the shaft, and J_{sum} is the total polar moment of inertia of everything on the shaft.

Another transient effect is heat soak in the turbomachinery. This is an effect whereby heat is soaked transiently from the gas path into the surrounding casing or vice versa. In a simple form, this effect is modeled by the following[1,6]

$$\dot{Q} = hA(T_{gas} - T_{met}) \tag{2}$$

$$\frac{dT_{mat}}{dt} = \frac{Q}{m_{mat} C_{p_{mat}}} \tag{3}$$

$$h_{gas,new} = h_{gas,old} - \frac{Q}{W_{gas}} \tag{4}$$

where T_{mat} and T_{gas} are the casing material (metal) and gas temperatures, Q is the heat transferred between them, A is the interface area, h is the heat transfer coefficient, m_{mat} is the mass of the metal, Cp_{mat} is the material's specific heat, W_{gas} is the gas path flow rate, and h_{gas} is the total enthalpy of the gas. The value of $h_{gas,old}$ is computed at the current time step in the parent element (usually after map look-ups), then $h_{gas,new}$ is calculated from the above equation and the parent element updates the gas properties using the newly computed enthalpy and another independent intensive property. An effect related to heat soak is transient tip clearances between the rotors and the surrounding case as the different materials expand and contract differently as temperature fluctuates. Unfortunately, this effect is difficult to model separately. Often this effect is an empirical modification to the turbomachinery map values, but is not included in the current effort because the required data was unavailable.

The effect of humidity within the turbomachinery is often a small effect, but can be implemented using some ratios that relate the true gas properties within a component (gas constant and ratio of specific heats) to those values that were assumed for the maps. The result is scalar map correction terms for speed, flow, and pressure ratio[7]. Another effect that is usually minor (though not always the case at high altitudes) is the Reynolds number (Re) effects. This effect is similarly implemented as scalar map correction terms for flow and efficiency as a result of derived and empirical formaulations.[8]

Because a change in fuel flow is not realized in the combustor instantly when a change command is issued, it is reasonable to implement a delay and/or lag in the combustion process. This can be implemented in the following manner:

$$W_{f_{actual,t}} = W_{f_{actual,t-\Delta t}} + \left(\frac{\Delta t}{\tau}\right) * \left(W_{f_{CMD,t-n\Delta t}} - W_{f_{actual,t-\Delta t}}\right) \tag{5}$$

where $W_{f_{actual,t}}$ and $W_{f_{actual,t-\Delta t}}$ are the actual fuel flow into the combustor at the current and previous model time step, $W_{f_{CMD,t-n\Delta t}}$ is the fuel flow requested n steps prior to the current time step, and τ is a time constant for the lag. An example of this effect, with τ=0.1s and n=10 (providing a pure time shift of 10ms for a 1ms Δt step time), is shown in Figure 2.

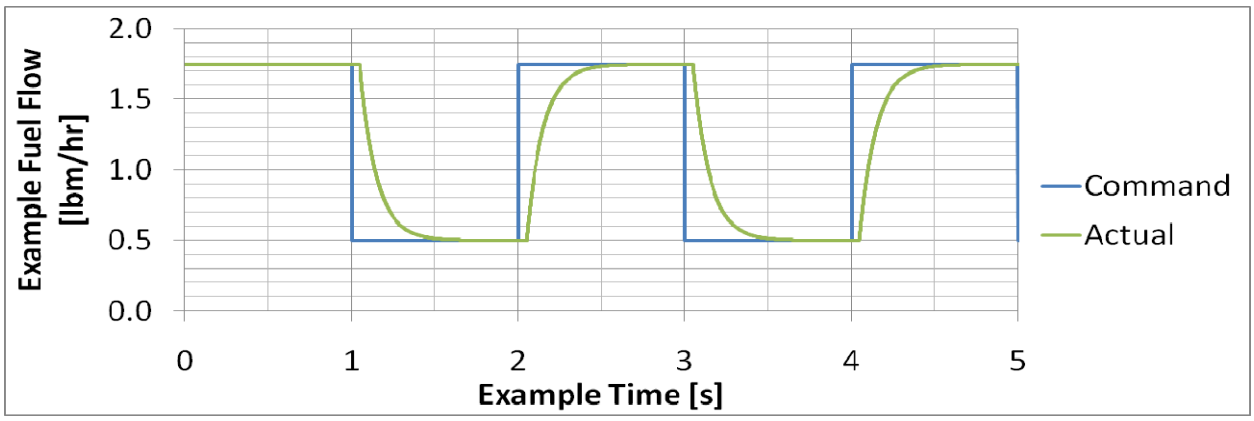

Figure 2: Representative fuel flow delay/lag.

There are other transient effects that are not captured in this effort: volume dynamics (volume packing) – the geometric information required was not available for a representative engine; heat transfer within multi-stage components – this is not easily included when compressors and turbines are represented as lumped 0-dimensional elements using maps; transient operation of engine variable features (i.e. capturing the changing area as the nozzle opens or closes) – this is control system dependent; inlet distortion effects – not easily implemented with a 0-dimensional fan; and transient performance of other variable geometry features of the engine – these are dependent on the control system and detailed information was not available.

2.2.3 Testing and Analysis

It is important to understand which dynamics are of appreciable value in modeling a VCE. Dynamics that significantly increase simulation time but do not add value in terms of fidelity or accuracy of the solution are not worth including. Clearly, including the shaft inertial effects are important rather than assuming an infinite ability to change instantaneously (as is the assumption for the quasi-steady-state approach of using a series of cycle balance points). This distinction is shown in Figure 3. The various figures in this section show the effect of each of the additional dynamic effects on the response of various engine parameters. In each of these figures, *Baseline* refers to the model when it includes only the shaft inertial effects. Other effects are assessed in reference to this effect alone: *Heat Soak* refers to the heat soak effect within turbomachinery in addition to inertial effects, *Re* refers to the Reynolds number corrections in addition to inertial effects, *Humidity* refers to the inclusion of moisture effects of the air in addition to inertial effects, and *Fuel Delay* refers to the effect of fuel flow delay/lag during transients with inertial effects.

Figures 3 through 11 illustrate a Bodie maneuver (also known as a "hot re-slam") performed at 35,000ft altitude and Mach 0.8. In the current work, this maneuver consists of a throttle chop from mil power to 50% of the mil power fuel flow, holding that low power setting for 5 seconds, and then a throttle slam back to mil power. Because an instantaneous change in fuel flow is unrealistic (even when not using the fuel flow delay/lag outlined in the previous section), the change was assumed to ramp linearly over 0.1s. Since the fuel flow change drives the response of the other variables, it is shown in Figure 4. It is apparent in this figure that the *Heat Soak* and *Humidity* lines are on top of the *Baseline* curve. The *Re* line has the same shape, but is slightly off in the steady-state values because this effect contributes both during transient and in steady-state. As expected, the *Fuel Delay* line is most noticeably different, taking approximately a half second to achieve the requested fuel flow at the new condition (both after the throttle chop and after the throttle slam).

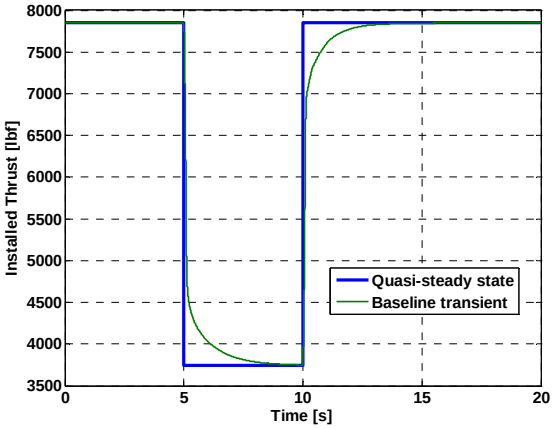

Figure 3: Quasi-steady-state versus inertial dynamics.

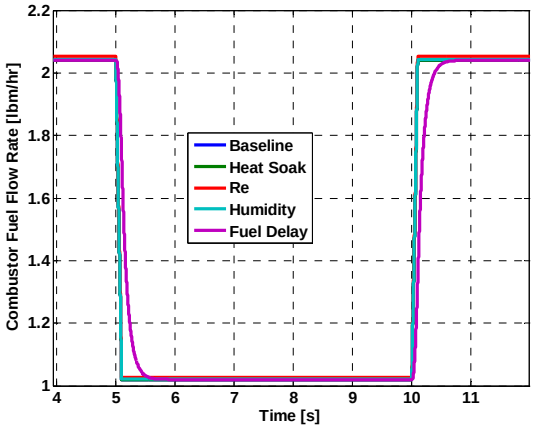

Figure 4: Actual (delivered) combustor fuel flow during 35kft altitude Bodie.

The engine operation during the Bodie maneuver is further illustrated in Figure 5, which shows the flow through each of the engine's flow paths during this transient. The top line shows the total engine airflow that enters the inlet. This value is held constant throughout the entire transient ("flow holding" by definition). However, the variable geometry features of the engine adjust the flow to the different paths during the transient. At time=0.0s, the flow is fairly evenly split between the core and the primary bypass, with comparatively little going through the third stream. However, when the engine is throttled back, much less thrust is required. To maintain the constant airflow, this air is dumped into the third stream. This low power condition is an example of an engine operation mode that has significant cooling capacity in the third stream. When the fuel flow rate is again increased, the core requires the additional air and the third stream flow is again reduced.

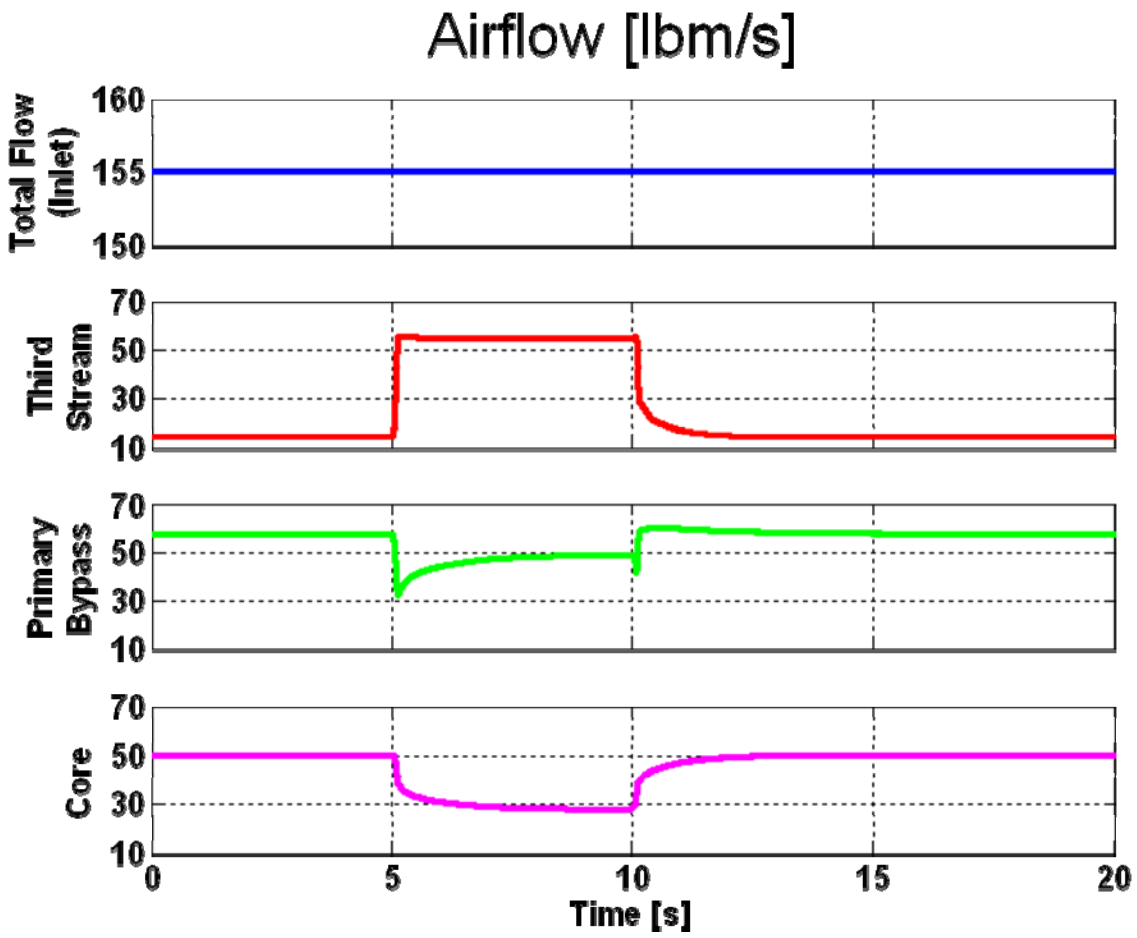

Figure 5: Airflow through each engine flow stream during 35kft altitude Bodie (*Baseline* case).

The installed thrust response through the Bodie maneuver is shown in Figure 6. This figure shows that there is not a substantial difference in this measure of overall performance between each of the cases. Another overall performance type variable, thrust specific fuel consumption (TSFC), also shows that most effects do not significantly impact this metric either. The exception is that the delayed fuel flow shaves off the maximum and minimum values of both the acceleration and deceleration events as shown in Figure 7.

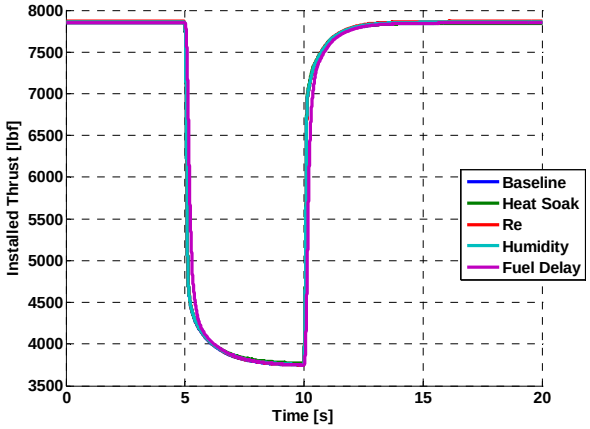

Figure 6: Installed thrust during 35kft altitude Bodie.

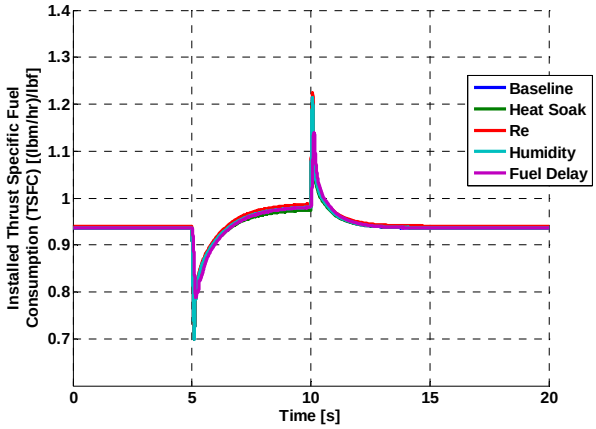

Figure 7: TSFC during 35kft altitude Bodie.

For some other parameters, the different effects are more pronounced. Figure 8 shows that the minimum high pressure compressor (HPC) stall margin varies by several percentage points based on which dynamic effect is captured. Similarly, temperatures differ based on the dynamics captured. Figure 9 shows the total temperature at the exit of the HPC, representative of the trends seen in the compression section temperatures. The heat soak effect is reasonably significant in this part of the engine. Figure 10 shows the inter-turbine total temperature. This is representative of temperature trends at stations in the hot section and as with the HPC stall margin, the peaks are reduced by the fuel flow delay/lag effect. The exhaust (from the primary nozzle) temperature is shown in Figure 11. This is similar to the trend at other stations downstream of the mixer.

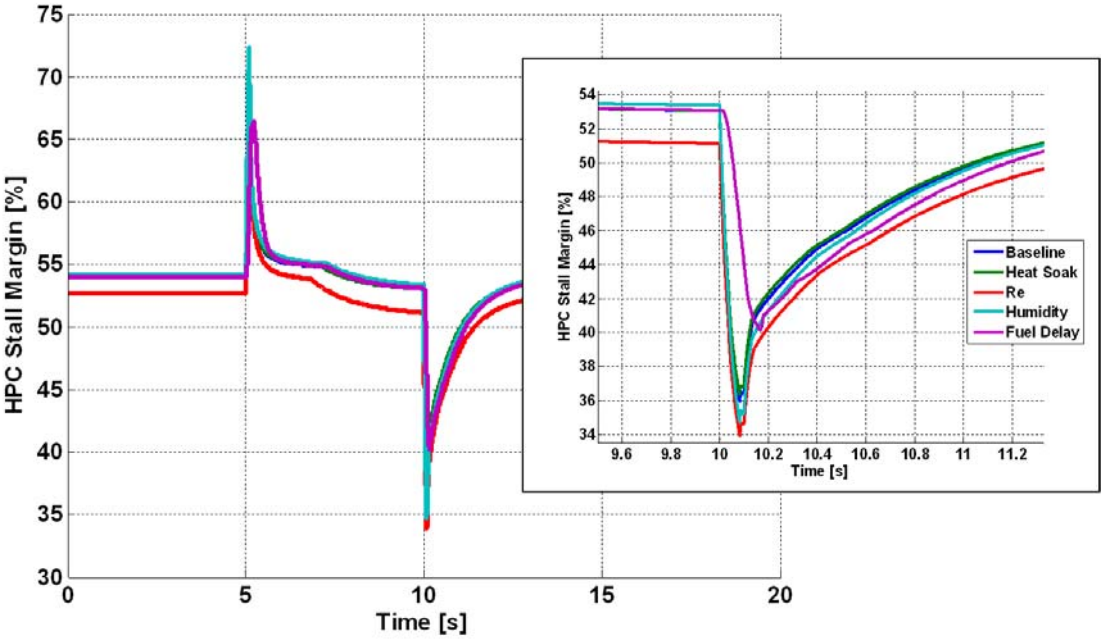

Figure 8: HPC stall margin during 35kft altitude Bodie.

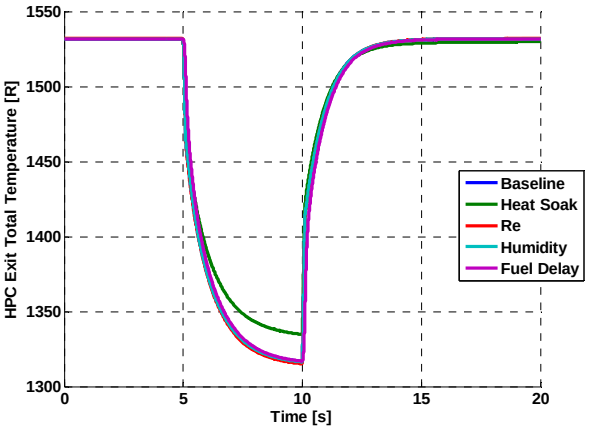

Figure 9: Compression section total temperature trends during 35kft altitude Bodie.

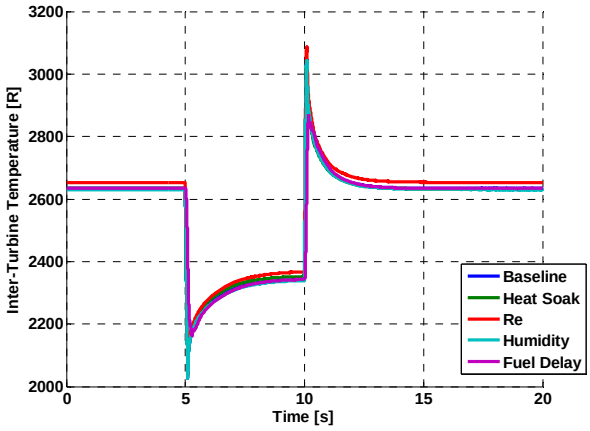

Figure 10: Hot section total temperature trends during 35kft altitude Bodie.

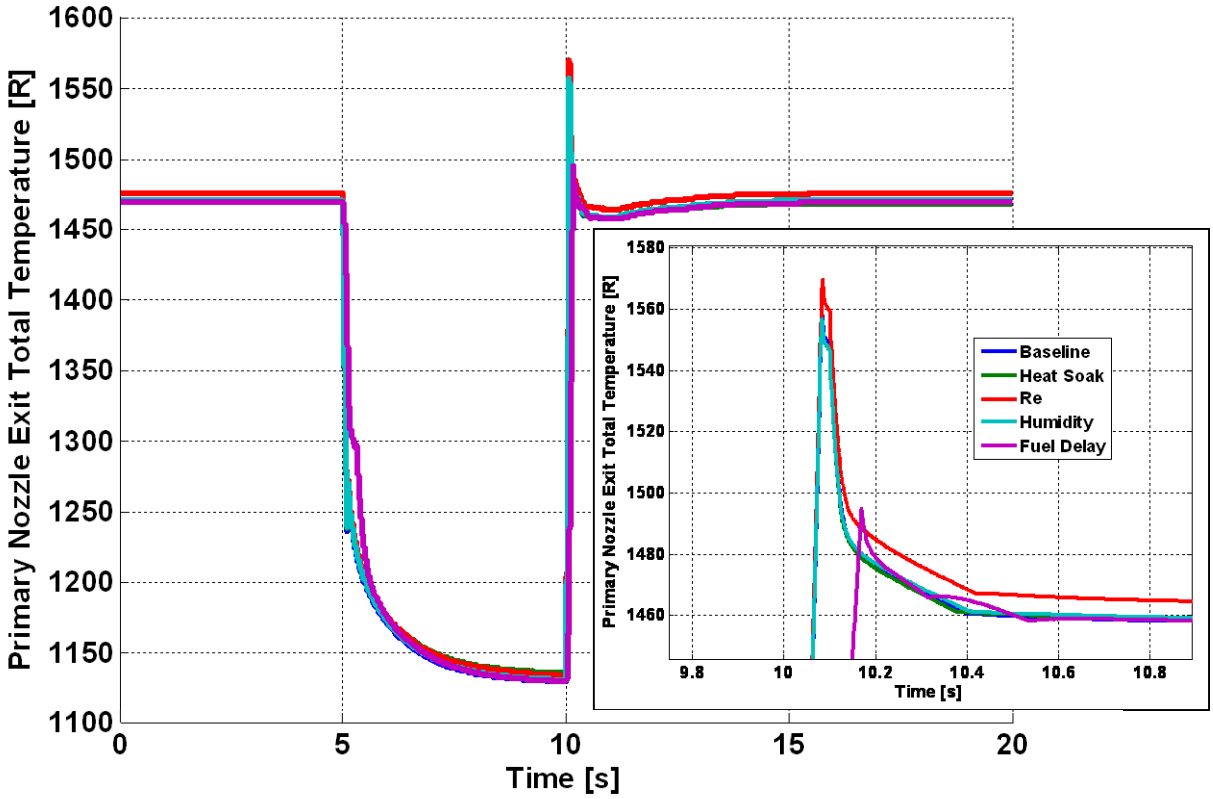

Figure 11: Primary nozzle exhaust temperature during 35kft altitude Bodie.

To assess the impact of air density on the transient effects, an additional altitude of 1,000ft (still at 0.8 Mach) is also considered. As a generalization, the engine was more responsive at the low altitude than at high altitude. As an example, the HPC stall margin transitions from its peak (high or low) value to its steady-state value more quickly. Additionally, the response of each of the transient effects differs slightly as shown in Figure 12, though the fuel delay/lag again brings the minimum stall margin up several percentage points. Figures 13 and 14 illustrate a difference in the shape of the response for corrected speed in the low pressure compressor (LPC). The 1,000 ft altitude case shows a faster arrival at the minimum speed than the higher altitude case, but it also illustrates the "overshoot" type response when including the heat soak effect. It is prudent to note that while the magnitude of the overshoot is tiny on an absolute scale, it represents an overshoot of about 2% relative to the difference between steady-state corrected speeds at the two fuel flow conditions.

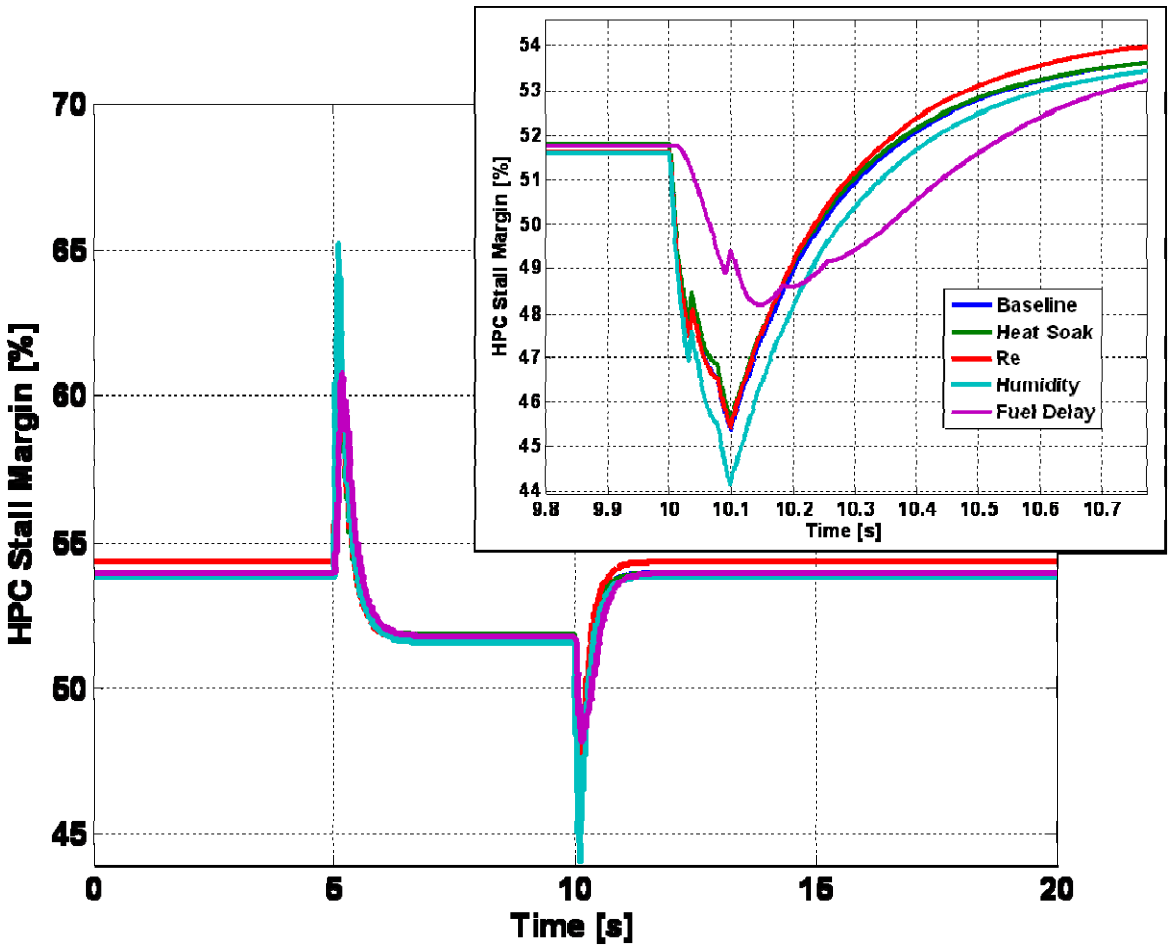

Figure 12: HPC stall margin during 1kft altitude Bodie.

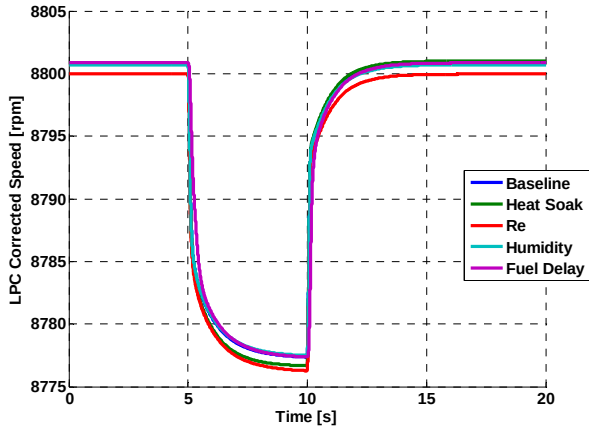

Figure 13: LPC corrected speed during 35kft altitude Bodie.

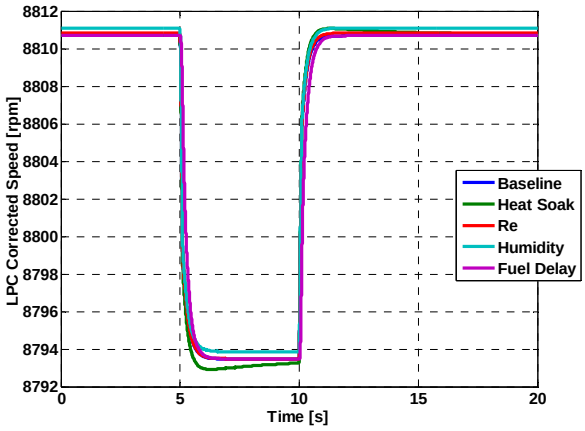

Figure 14: LPC corrected speed during 1kft altitude Bodie.

The impact of each of these transient effects on computational time is also important. If the simulation is required to run in real time (as would be necessary for hardware-in-the-loop), then the choice of including or excluding the dynamic effects can become critical. Similarly, for batch runs, simulation speed might be strongly preferred over accuracy. Table 1 shows the computational time required to run the same 20 second (simulation time) Bodie transient with each of the dynamic effects. With one exception, the NPSS built-in GEAR_2ND_ORDER solver was used. In the case of the *Humidity* effect, there was numerical instability in the GEAR_2ND_ORDER solver when the smaller time step was used. To alleviate this, the explicit EULER solver was used for that case instead. However, that makes it more difficult to compare directly with the other cases. Each case was run using both time steps of Δt=1ms and Δt=10ms and each was run multiple times then averaged.

It can be seen that there is generally only a minor effect on simulation time by adding the additional dynamic effects. In fact, not all cases displayed an increase in simulation time when the additional effects were included. The *Fuel Delay* case reduced computational time by an average of nearly 4% for the Δt=1ms time step case. This is due to the peak shaving effect noted above. Because the delayed fuel flow allowed the engine to miss the highest peaks and valleys for many variables, it required fewer iterations to converge at those time steps. With the two major transient events in the test (throttle chop and throttle slam), this added up to a noticeable time difference. As mentioned, the *Humidity* case with Δt=1ms did not run well with the same solver as the other simulations. Some of the other simulations, in turn, did not run well with the explicit EULER solver, so it was difficult to compare directly. The change of solver is largely credited with the speed increase in that case, but it should neither be assumed that the EULER solver is always faster nor that the EULER solver is more stable in all cases.

Table 1: Simulation timing.

Test	Mean Time for Δt=1ms	% Delta	Mean Time for Δt=10ms	% Delta
Baseline	47.64	0.00	5.37	0.00
Heat Soak	51.42	7.93	5.51	2.57
Humidity	42.32*	-11.17*	5.28	-1.71
Re	47.92	0.59	5.06	-5.74
Fuel Delay	45.76	-3.95	5.40	0.63

*=EULER solver used for Δt=1ms *Humidity* case

While the cases with a larger time step also displayed some instances where the additional dynamics improved runtime, caution should be used since the computational time for the worst case was required less than half a second more than the fastest case. Additionally, the accuracy of the solution at the larger time steps was reduced, which likely led to missing the peaks (again reducing the number of iterations required). Adding all dynamic effects at the same time may not produce a predictable increase in simulation time. In the current work, the various effects were not combined into an all-inclusive case.

Based on these general timing results, it is roughly computationally neutral whether to include the additional effects or not. For this reason, it is logical to include them if the appropriate information is available. As a cautionary note, the *Fuel Delay* approach implemented here is crude and would be much more appropriately handled as part of a FADEC model. A FADEC would also be of vital importance for stability studies since it imposes limits to avoid stalling or surging the compressors and fans.

A different type of transient was also considered in this effort. This involved constant fuel flow at the higher altitude condition (35,000 ft, 0.8 Mach), but instead varying the shaft power extraction. Obviously at a constant fuel flow, the *Fuel Delay* test would be identical to the *Baseline* case so it was not considered for this portion. A base loading of 50hp from the LP spool and 7.5hp from the HP spool was used. An additional large 700hp load was applied to either the LP or HP shaft over 5ms (linearly). The large load was also removed in the same manner, returning to the base load. This study considers only one "load on" event and one "load off" event; pulse loading (e.g. for a high power radar) may be considered in future studies in a similar manner. Figures 15 and 16 show the installed thrust for the large step load being applied to the HP shaft or the LP shaft, respectively. Both of these figures show more difference between the various dynamic effect cases than the Bodie transient did. This is due to the fuel flow being constant throughout the test, but not the same for each of the tests. There were different initial conditions when each case was run (after the design and off-design steady state points). Therefore, as a qualitative conclusion, the additional transient effects do not contribute significant changes to the shape of the transient for either the HP or LP shaft loading. As can be seen by comparing Figures 15 and 16, there is a slight thrust benefit in the "load on" state when extracting the 700hp from the LP spool rather than the HP spool. This similarly translates to a slightly more favorable TSFC for the LP extraction case. The slopes of the thrust curves as the load comes on and off suggest that the engine is more greatly impacted (or at least more quickly impacted) when the load is applied to the LP shaft. It is important to note that a more likely test would include the FADEC compensating for the loss is thrust (or other control signal) by increasing fuel flow. This effect was not modeled in this work.

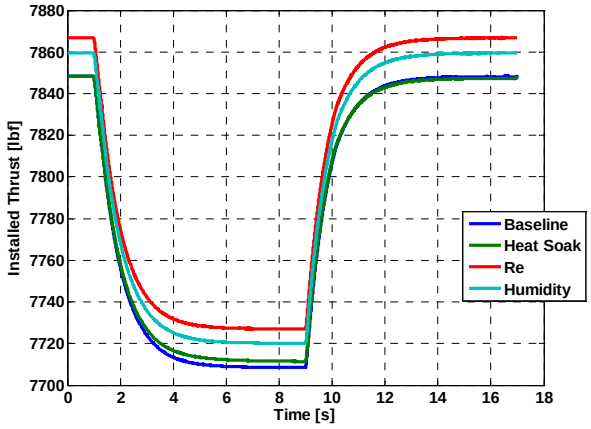

Figure 15: Installed thrust during HP shaft loading transient.

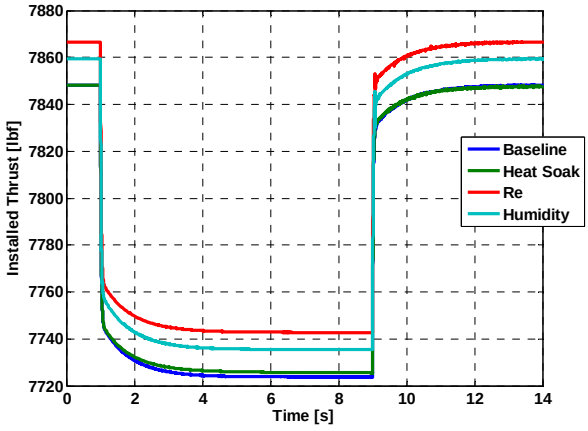

Figure 16: Installed thrust during LP shaft loading transient.

2.3 Fuel Thermal Management System

The fuel thermal management system (FTMS) on board modern more electric aircraft provides a significant heat sink for aircraft loads. Through use of fuel-oil loops, heat is rejected through heat exchangers from on-board mechanical/electrical loads to the fuel with the goal being to maximize the temperature of the fuel at the engine combustor, thus maximizing the fuel's heat sinking capability. Predicting how these fuel temperatures vary throughout a mission is essential to determining potential problems regarding overheating of aircraft components and/or exceeding fluid temperature constraints.

The fuel tank model was derived using a single node approach for the fuel and ullage, and a finite-volume calculation for the fuel tank walls. Convective heat transfer is assumed between the fuel and walls, the ullage

and walls, and the fuel and ullage. The convective rate is determined by the temperature differential, fixed heat transfer coefficients for the dry and wetted portions of the wall, and a surface area that is dependent on the amount of fuel in the tank. The time derivative used to determine fuel temperature is given by:

$$\rho V C_p \frac{dT_f}{dt} = \sum_{i=1}^{n} h_i A_i \left(T_i - T_f\right) + \dot{m} C_p \left(T_{in} - T_f\right) + h_{fg} A_{fg} \left(T_g - T_f\right) \tag{6}$$

where the incoming flow can be from any upstream tanks or additional sources. The ullage temperature can be solved by the following:

$$\rho V C_p \frac{dT_g}{dt} = \sum_{i=1}^{n} h_i A_i \left(T_i - T_g\right) + h_{fg} A_{fg} \left(T_f - T_g\right) \tag{7}$$

The fuel-gas interface area can also change as the fuel tank drains. All wall area maps are loaded into the model from a spreadsheet.

A second component, the Tank Environmental Interface (TEI), is used to determine the temperatures at each of the fuel tank walls' interior surfaces. The TEI block utilizes a finite-volume calculation to determine transient heat transfer through the wall and/or aircraft skin. The external surface calculation allows for convection, infrared radiation, and radiation absorption in the solar band. The interior surface calculation has a convective boundary condition.

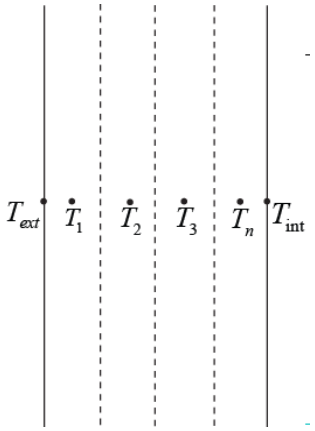

Figure 17: Finite-volume discrete material thicknesses.

The finite-volume approach allows for multiple material layers to be used without need for a structured mesh.[9] To determine conduction between materials whose thermal conductivities are not equal, a harmonic mean is used that is a function of each material's thermal conductivity and thickness between the node and interface location. The thermal conductivity of an interface is given by:

$$k_{if\,1-2} = \frac{\Delta x_{if_1} + \Delta x_{if_2}}{\frac{\Delta x_{if_1}}{k_1} + \frac{\Delta x_{if_2}}{k_2}} \tag{8}$$

As previously stated, the external surface temperature calculation allows for both convective and radiative heat transfer. Due to the fourth power term from infrared radiation, an iterative solution is required. A Newton-Raphson iteration is used to solve for the external surface temperature as follows:[10]

$$h\left(T_{conv}-T_{ext}\right)+\varepsilon\sigma\left(T_{rad}^4-T_{ext}^4\right)+\alpha Q''_{sol}+\frac{k}{\Delta x}\left(T_1-T_{ext}\right)=0 \tag{9}$$

The surface temperature for each iteration is given as:

$$T_{ext}^{k+1}=T_{ext}^{k}-\frac{f\left(T_{ext}^{k}\right)}{g\left(T_{ext}^{k}\right)} \tag{10}$$

where

$$f\left(T_{ext}\right)=hT_{ext}+\frac{k}{\Delta x}T_{ext}+\varepsilon\sigma T_{ext}^4-\left(hT_{conv}+\varepsilon\sigma T_{rad}^4+\alpha Q''_{sol}+\frac{k}{\Delta x}T_1\right) \tag{11}$$

$$g\left(T_{ext}\right)=h+\frac{k}{\Delta x}+4\varepsilon\sigma T_{ext}^3 \tag{12}$$

Although models that require iterative solves for every time step can be computationally inefficient, the observed convergence typically required less than 5 iterations, and therefore the solution was not a computational burden, and linearization (a common practice for radiation problems) was not necessary.

Assuming a linear temperature profile between nodes, the time derivative for interior nodal temperatures is calculated based on conduction between adjacent nodes as:

$$\rho_i\Delta x_i C_{p,i}\frac{dT_i}{dt}=\frac{k_{if_{i-1}}}{\Delta x_{if_{i-1}}}\left(T_{i-1}-T_i\right)+\frac{k_{if_i}}{\Delta x_{if_i}}\left(T_{i+1}-T_i\right) \tag{13}$$

A heat transfer coefficient and tank temperature is input to the TEI model from the fuel tank, and the interior surface boundary condition is calculated as:

$$T_{wall}=\frac{hT_{\text{tank}}+\dfrac{k}{\Delta x}T_n}{h+\dfrac{k}{\Delta x}} \tag{14}$$

The Simulink numerical integration solvers are used to determine the interior node temperatures at each time step, and a while-loop subsystem is used to provide multiple Newton-Raphson iterations at a given time step. The approach above provides an increased level of fidelity above traditional steady-state solutions, while maintaining computational efficiency. An example study conducted with a six wall fuel tank/TEI combination containing 20 continuous states completed a 240 minute mission in approximately one second.

Next, it is necessary to determine the input parameters to the boundary conditions in Eqn. 9. The external surface is exposed to air flow over the wing surface, and Mach number and altitude dependent air properties. The toolset provides the user with a range of air properties commonly used in aircraft modeling, and

calculates the air property variations as a function of altitude, Mach number, day type, time of day, date, and latitude. These parameters can be used to determine external convective temperatures, such as the adiabatic wall temperature[11] that is given as:

$$T_{ad} = T_{amb}\left[1 + P_r^{1/3}\left(\frac{\gamma - 1}{2}\right)M^2\right] \tag{15}$$

In combination with the adiabatic wall convective temperature, a flat plate heat transfer coefficient calculation is available to the user, with the input being the effective flat plate length. From this, the Nusselt number for laminar and turbulent flow is given as:

$$Nu_l = \begin{cases} 0.664 P_r^{1/3}\,\mathrm{Re}_l^{1/2} & \text{for } \mathrm{Re}_l < 5\times10^5 \\ 0.0296 P_r^{1/3}\,\mathrm{Re}_l^{1/2} & \text{for } \mathrm{Re}_l \geq 5\times10^5 \end{cases} \tag{16}$$

and the heat transfer coefficient is calculated as:[12]

$$h = \frac{Nu_l k}{x_l} \tag{17}$$

The radiation parameters at the surface must also be determined. To account for the solar diurnal cycle along with location/time of year dependence, a solar declination angle is determined along with a zenith angle. The declination angle is based on the day number (1-365):

$$\delta = 23.45\sin\left(\frac{360}{365}(284 + N)\right) \tag{18}$$

and the subsequent zenith angle can be calculated from:

$$\cos(\theta_z) = \cos(h)\cos(\delta)\cos(\phi) + \sin(\phi)\sin(\delta) \tag{19}$$

where ϕ is latitude and h is the solar hour angle.[13] The actual solar irradiance can be calculated from:

$$Q''_{sol} = Q''_{sol,\max}\cos(\theta_z) \tag{20}$$

The maximum solar irradiance increases with increasing altitude. Underneath the aircraft, the solar irradiance is the amount reflected off the clouds or earth, this reflection value is set by the user. Depending on the mission profile, significant changes in latitude and/or relative solar hour angle will occur; the model supports integration of mission specific table lookups to specify latitude and solar hour angle versus time if the added fidelity is desired.

Infrared radiation must also be accounted for at the surface; there is an emitted component that is a function of the aircraft surface temperature, and an absorbed component from the effective sky temperature. Molecules in the atmosphere absorb both solar and infrared radiation, and this energy is emitted in the infrared band as well. The number of molecules decreases with increasing altitude, and therefore the effective sky temperature decreases with altitude until the tropopause is reached, after which the sky radiation temperature is approximately constant up to an altitude of 12 miles. Typical sky radiation temperature lapse rates are a

decrease in temperature of 3.57°R per 1000 ft, with a fixed temperature of 390°R above 36000 ft, and below 64000 ft.[14] Underneath the aircraft the bottom surface radiation temperature will be that of the earth or clouds while at altitude, and the temperature of the runway while at ground hold. Attenuation in infrared radiation emitted from the earth or clouds can be accounted for through modification of the underlying code.

Through the TEI block mask, the user has the ability to select for each wall to be modeled the radiation parameters at the surface (infrared emissivity, solar absorptivity, top or bottom surface, no radiation), convective parameters (heat transfer coefficient calculation, convective temperature), and wall material type (how many layers, material type and thickness per layer). Proprietary aircraft skin material types can be loaded into the model through a user specified spreadsheet.

A generic fuel tank was modeled over a 240 minute mission. The aircraft sits at ground hold for the first 60 minutes, climbs to cruise at 30kft, performs a supersonic (Mach 1.2) dash at 120 minutes at 25kft, lands shortly after at 135 minutes and sits at ground hold for an additional 105 minutes. The tank is drained to a minimum fuel mass of 60 lbs at 120 minutes. The external air properties are based on a 5% hot day, location is at the equator during the vernal equinox, start of mission at 10:00 AM. The results are shown below for the top and bottom skin surfaces along with the resulting fuel temperature over the mission.

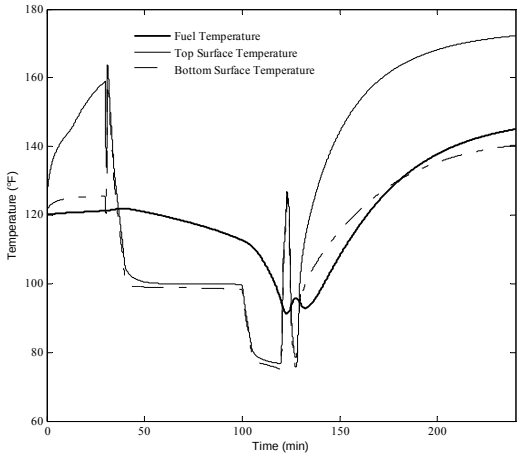

Figure 18: Fuel tank temperature and skin surface temperatures outside of fuel tank walls.

The top surface heats up significantly during the first 60 minutes of the mission, primarily a result of solar heating and decoupling with the fuel due to tank drain. The bottom surface heats up primarily as a result of the infrared radiation from the 140°F runway, but due to full coupling with the fuel, the temperature increase is not as significant. The fuel temperature prediction is essential in predicting the worst case TMS condition needed for TMS sizing/design.

2.4 Environmental Control System

The model of the Environmental Control System (ECS) is considered next. This includes air cycle machine components (compressor, turbine, water separator, aspirator, duct, heat exchanger, and ejector) and heat sources such as the cockpit and equipment bay models that can calculate heat transfer through the aircraft skin and from internal sources, and predict the amount of air flow required to maintain temperature constraints.

The size of the ECS is driven by the amount of cooling required by the equipment bays, cockpit, and any other air cooled components. Equipment bays are often exposed to heat transfer through the aircraft skin, and like the fuel tank, capturing the time history of thermal energy transferred to the bay is essential in predicting the worst case operating condition. To this end, the TEI model was modified and integrated with a single node to predict bay temperature. The finite-volume code is implemented to predict internal wall surface temperatures. The time derivative of the bay temperature is written as,

$$\rho V C_p \frac{dT_{bay}}{dt} = \sum_{i=1}^{n} h_i A_i \left(T_i - T_{bay}\right) + \dot{Q}_{\text{int}} + \dot{m} C_p \left(T_{in} - T_{bay}\right) \tag{21}$$

where each wall's heat transfer coefficient is based on the user specified sea-level value and ambient bay pressure, and $\dot{Q}_{\text{int}}$ relates to any internal heat loads from mechanical or electrical systems. To predict the required inlet air flow rate needed to maintain a user specified temperature for a given operating condition, the time derivative is set to zero and air flow rate is solved for as,

$$\dot{m} = \frac{\sum_{i=1}^{n} h_i A_i \left(T_i - T_{desired}\right) + \dot{Q}_{\text{int}}}{C_p \left(T_{desired} - T_{in}\right)} \tag{22}$$

The effective bay cooling requirements can be determined from the desired bay temperature, inlet temperature, and flow rate from Eqn. 22. A test case was run wherein a constant 2.5 kW heat load is applied inside the bay. The same 240 minute mission from Figure 18 is flown and the cooling requirements for the bay are predicted and shown in Figure 19.

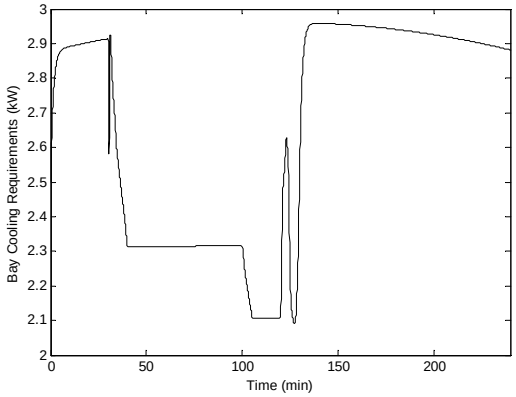

Figure 19: Bay cooling requirements.

During ground hold conditions, the cooling requirements are greater than that of the bay heat load due to external heating of the aircraft surface. While in flight, the effective bay cooling requirement is less than that of the internal load as some of the heat is sinked to the external environment. Another significant heat load in the ECS is the cockpit.

The cockpit contains several heat transfer mechanisms similar to that of the bay, with the primary difference being solar transmission through the canopy material. The user can specify the projected solar transmission

area. The external canopy surface will have external radiation and convection. As in the bay model, there are internal heat loads, including electronics and pilots, and cooling air requirements are predicted. To calculate heat transfer into the cockpit from the external environment, Eqns. 9 and 13 are used for the canopy external surface and internal material respectively.

The heat stored in the canopy is transferred into the cockpit through convection. The cockpit temperature is calculated as in Eqn. 21 and the required air flow rate to maintain a comfortable cockpit temperature is calculated using Eqn. 22.

A test case was considered wherein the mission from Figure 18 was run for a large cockpit with a projected area of 30 ft^2, and two occupants; the required cockpit cooling rate was determined (Figure 20). The cockpit has a constant 500 watt load from internal electronics, and each occupant has a heat load of 120 watts.

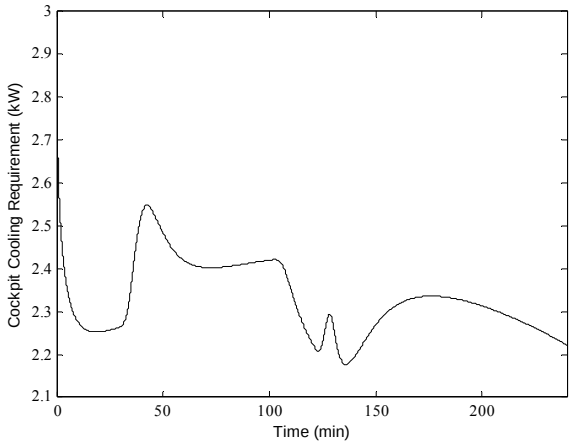

Figure 20: Cockpit cooling requirements.

The internal heat generation from the pilots and electronics totals 740 watts, and from Figure 20 it is clear that the required cooling is significantly greater than that. This is due in large part to the significant size of the cockpit, and therefore the large amount of solar transmitted. With the cockpit and bay models, the user can predict the cooling power requirements for the ECS over the entire mission and evaluate the worst case sizing condition.

2.5 Power Thermal Management System

The PTMS employs a closed circuit air refrigeration cycle to regulate the aircraft's liquid cooled avionics, air cooled avionics and cockpit heat loads. The closed circuit air refrigeration architecture makes use of three air circuits: bleed air circuit (purple), closed loop air circuit (red), and open loop air circuit (blue) (Fig. 21). The purpose of the bleed circuit is to provide high pressure air from the engine to the power turbine (PT) or integrated power package (IPP). The bleed air from the main engine is expanded by the power turbine and useful work is generated to operate the refrigeration cycle. The bleed air circuit provides the make-up air for the open loop air circuit.

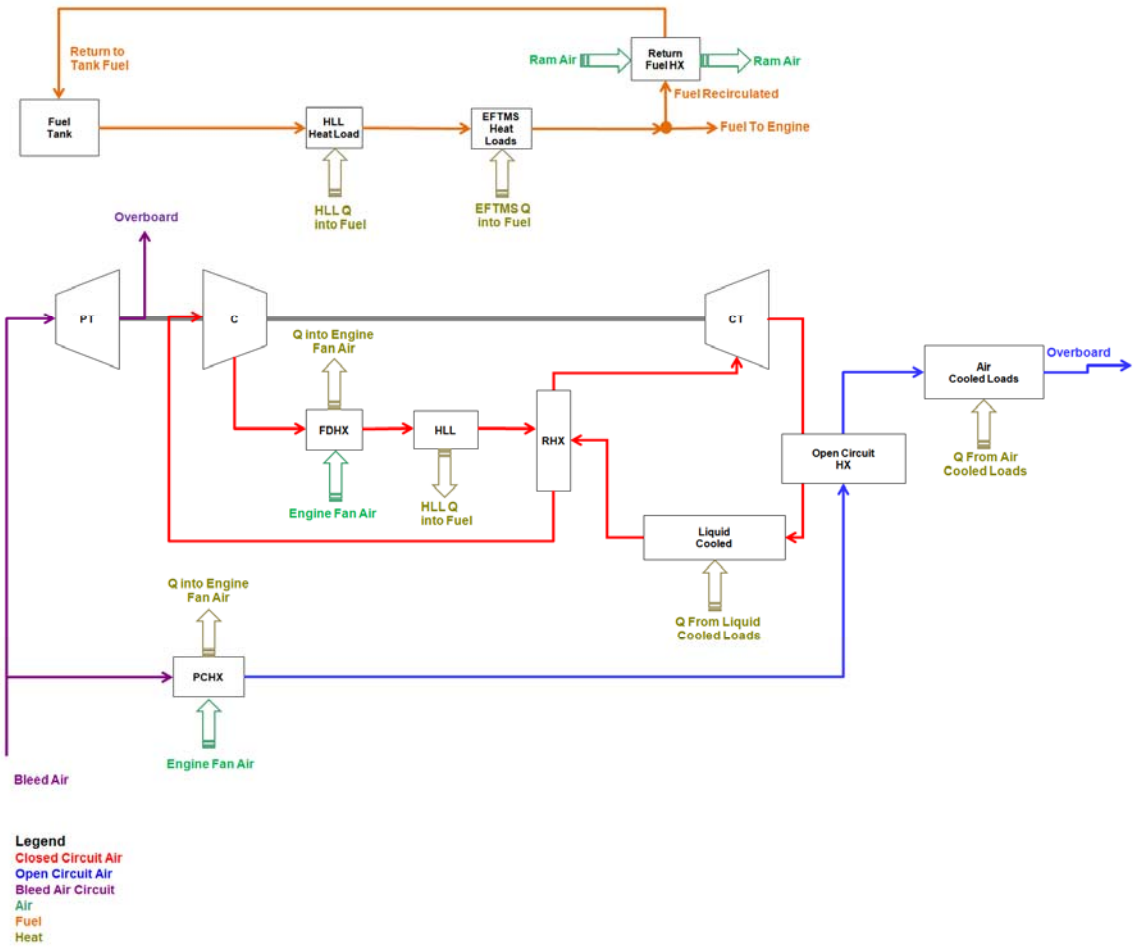

Figure 21: Thermal Management System Architecture.

The closed refrigeration circuit is used to cool both the liquid cooled loads as well as to cool the open loop air stream. The closed refrigeration circuit operates by expanding compressed air in the cooling turbine (CT) resulting in refrigerated air. The refrigerated air is used to absorb the heat loads from the liquid cooled avionics as well as the open loop air circuit. The refrigerated air interfaces with the aircraft's liquid cooled avionics through a PAO loop which transfers the heat generated by the avionics to the low temperature expanded air stream. After absorbing the heat loads, the expanded air stream is used by the counter flow air to air recuperator heat exchanger (RHX) to reduce the temperature of the high pressure air stream from the compressor.

The compressor (C) is employed to raise the pressure of the air stream. The high temperature air stream is cooled by sinking heat to the environment which lowers the air stream temperature. The closed refrigeration circuit uses two heat exchangers to remove heat from the high pressure and temperature air stream. The primary heat sink is the fan duct heat exchanger (FDHX), which continuously operates when the main engine is operating. The FDHX is located in the fan stream of the main engine. An additional hot liquid loop (HLL) is used as a supplementary heat sink. In conditions when the heat load regulation temperatures are exceeded, the supplementary heat sink is engaged. The hot liquid loop is a PAO loop which sinks the high pressure, high temperature closed loop air stream to the aircraft fuel.

The fuel circuit pumps fuel from the aircraft fuel tanks to the engine. In the pumping process heat is absorbed from the Full Authority Digital Engine Control (FADEC), PTMS, and EFTMS among other heat loads. The return to tank logic regulates the fuel and engine oil temperatures below their maximum threshold values. The EFTMS commands additional fuel flow if either the fuel or oil temperature thresholds are exceeded. The fuel not used by the engine is returned to the aircraft fuel tanks. The returning fuel is cooled by the return fuel heat exchanger (RFHX) before returning to the fuel tanks. The FADEC heat load is the initial heat load absorbed by the fuel. The FADEC has strict temperature limits which in turn results in strict temperature limits imposed on the fuel leaving the fuel tanks.

2.5.1 Integrated Power Package

The IPP, shown in Figure 22, is located within the PTMS architecture and is responsible for cooling the air cooled avionics, cockpit, and liquid cooled avionics. Consisting of a power turbine, closed loop compressor, and closed loop turbine, the IPP uses high pressure bleed air from the main engine compressor to power a closed loop air cycle. The IPP speed control valve, located between the IPP power turbine and the main engine compressor, regulates the mass flow of high pressure bleed air from the main engine compressor to the IPP. When the control valve is fully open, all available bleed air is sent to the IPP's power turbine and the cooling capacity of the closed loop air cycle is maximized. As the control valve closes, overall mass flow of bleed air to the IPP's power turbine is reduced and the cooling capacity falls. The IPP speed control valve is operated to maintain a POA oil temperature of 60°F in the liquid cooled avionics loop. A PI controller measures the actual temperature of oil entering the liquid cooled avionics, compares this value to the set point value of 60°F, and then operates the IPP speed control valve accordingly until the difference between the actual and set point temperatures is zero.

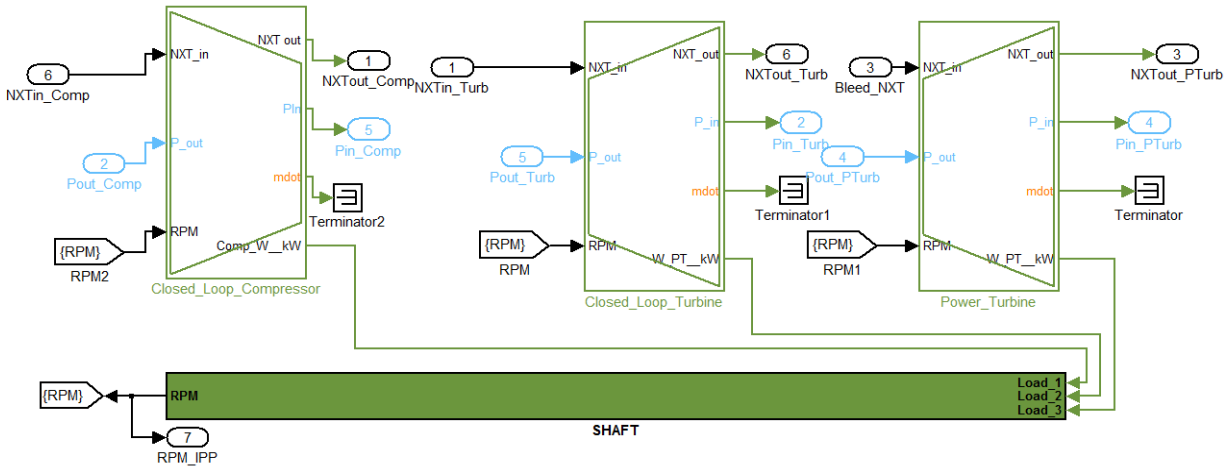

Figure 22: Transient IPP Simulink Model.

In order to capture dynamics within the IPP model, two different approaches are employed. First, an inter-component volume method is used by modeling a plenum volume after each of the different turbomachinery models. In the case of the IPP, plenum volumes are placed after the power turbine, closed loop compressor, and closed loop turbine. The turbomachinery models contain generic performance maps that can easily be based on experimental data. These maps are a function of shaft speed, pressure ratio, and inlet conditions, such as temperature and molar composition of the incoming air, and output a corrected mass flow. With the

incoming and outgoing mass flows of the plenum volume known, the dynamic pressure of the plenum volume can be calculated via integration of the ideal gas law, as shown by Eqn. 23.

$$P = \int \frac{(\dot{m}_{in} - \dot{m}_{out})RT}{V} dt \tag{23}$$

Secondly, the IPP model considers shaft inertia. Any changes in torque to the IPP shaft will vary the shaft speed. By considering the shaft inertia, however, this variation does not occur instantaneously. This time delay is captured in the model, once again demonstrating dynamic capabilities.

2.5.2 Heat Exchangers

Dynamic heat exchanger models have also been developed for use with the PTMS model. The heat exchanger models used in previous modelling efforts were predominately steady-state, which are easy to use and comprehensive. In steady-state heat exchangers, all energy is immediately transferred from one fluid to the other. In reality, the heat exchanger medium must be considered, as the heat exchanger mass stores and supplies heat depending on the perturbation. In order to create transient models, the material characteristics of the heat exchanger itself must be considered.

The heat exchanger is divided into three separate nodes. These nodes allow the user to obtain more detailed temperature distributions through the heat exchanger medium as well as create a counterflow heat exchanger. Each of the three nodes contains blocks that are used to model energy flow within the heat exchanger. A block is present for each of the two fluid streams and a third block represents the heat exchanger medium. The energy balance calculations completed in each of the fluid streams are shown in Eqns. 24 to 27. These outgoing fluid temperatures are sent to the heat exchanger medium block. Similarly, the heat exchanger medium block computes an energy balance and relays the heat exchanger temperature to the fluid stream blocks, shown by Eqn. 28. These temperatures are made transient through the integration at the end of each energy balance calculation.

$$\dot{q}_{HX} = hA(T_{oil} - T_{HX}) \tag{24}$$

$$\dot{e}_{in} = \dot{m} c_{p_{in}} T_{oil_{in}} \tag{25}$$

$$\dot{e}_{out} = \dot{m} c_{p_{out}} T_{oil_{out}} \tag{26}$$

$$T_{oil_{out}} = \int \frac{\dot{e}_{in} - \dot{e}_{out} - \dot{q}_{HX}}{V_{HX} \rho_{out} c_{p_{out}}} dt \tag{27}$$

$$T_{HX} = \int \frac{\dot{q}_{net}}{m_{HX} c_{p_{HX}}} dt \tag{28}$$

All heat exchangers are modeled as tube and shell type heat exchangers. Each heat exchanger model is masked and calls for the user to input key physical parameters, such as tube diameter, heat exchanger material capacity, heat exchanger mass, heat exchanger volume, and the heat exchanger cell area.

The heat transfer coefficients shown in Eqns. 24 to 27 have been made fluid dependent. Using physical parameters specified by the user, the Reynolds number is calculated for each stream. The Nusselt number is

calculated using the Dittus-Boelter equation, Eqns. 29 and 30. The convective heat transfer coefficient is then derived using the thermal conductivity and diameter of the heat exchanger tube, as shown by Eqn. 31.

$$For\ Re \geq 10{,}000,\ Nu = .023Re^{4/5}Pr^{n} \qquad For\ Re \leq 10{,}000,\ Nu = 3.66 \tag{29}$$

$$For\ T_s > T_m,\ n = 0.4 \qquad For\ T_s < T_m,\ n = 0.3 \tag{30}$$

$$h = \frac{Nuk}{D} \tag{31}$$

The heat exchanger mask prompts the user to select a fluid type for both the hot and the cold streams. The fluid selection is linked to polynomial function blocks that determine fluid properties as a function of temperature throughout the models.

2.5.3 Fuel and Oil Pumps

A quasi-steady-state pump model is utilized, meaning the pump inertia is not considered. This model is used for both the engine fuel and oil pumps. The model is designed so that pump speed is directly related to engine speed through an assumed constant gear ratio. In addition, the change in pump speed also leads to the generation of heat that is then rejected to the fluid stream. The TMS is designed to dissipate these time-variant heat loads. In fact, the pumps are a significant heat source for the FTMS loops.

The performance characteristics of these pumps are represented by generic maps stored in a spreadsheet. This simplification is sufficient for determining the transient heat loads of the pumps throughout the mission and is the standard industry approach. This data can be populated with experimental pump data by the user. These maps contain mass flow rate data as a function of pressure ratio and rotation speed as shown in Eqn. 32.

$$\dot{m} = f\left(\frac{P_{out}}{P_{in}}, N_{shaft}\right) \tag{32}$$

This mass flow is used to calculate the pump work, which then leads to the heat generation through Eqn. 33. The fluid temperature rise is the computed using the energy balance of Eqn. 34.

$$\dot{q}_{pump} = \dot{m}_{pump}(\eta_{pump} - 1) \tag{33}$$

$$T_{fluid_{out}} = T_{fluid_{in}} + \frac{\dot{q}_{pump}}{\dot{m}c_p} \tag{34}$$

2.5.4 Engine Oil Heat Rejection

Similarly to the fuel and oil pumps, the heat rejected directly from the engine to the oil can be significant. The engine oil heat load is physically modeled. This is done by creating an oil loop that interacts with four heat transfer nodes representing the engine fan, compressor, low-pressure turbine, and high-pressure turbine shaft bearings. This oil loop absorbs heat from each of these bearings in parallel and then transfers this heat to the fuel stream through an additional heat exchanger.

The heat transfer at each of these four nodes is determined with Eqn. 35 using the temperature difference between the oil and the bearing node. The temperature data at each engine station comes directly from the engine model.

$$\dot{q}_{node} = hA(T_{oil} - T_{node}) \tag{35}$$

This temperature data, along with known heat transfer values for various mission segments, enabled the initial selection of the four heat transfer coefficients.

2.6 Compact Heat Exchanger

While not utilized in the model results presented in this manuscript, a detailed description of a compact heat exchanger design system will be given. AFRL plans to investigate trade studies analyzing the benefits of integrating compact heat exchangers into the TMS. Based on the results of these trade studies, compact heat exchangers will be utilized as appropriate. A representative compact plate-fin heat exchanger is shown in Figure 23. The process used to construct the compact heat exchanger model can be broken into two steps:

1) Size the heat exchanger:
   a) Create an algorithm that calculates the weight and volume of the compact heat exchanger based off the physical and operational parameters.
   b) Minimize the weight of the heat exchanger using the appropriate physical and operational constraints

2) Construct the heat exchanger model:
   a) Formulate the equations governing the thermodynamic performance of the heat exchanger and ensure that the new model uses the correct correlations to determine heat transfer coefficients.
   b) Validate model by comparing the results obtained from simulations to data found in the literature.

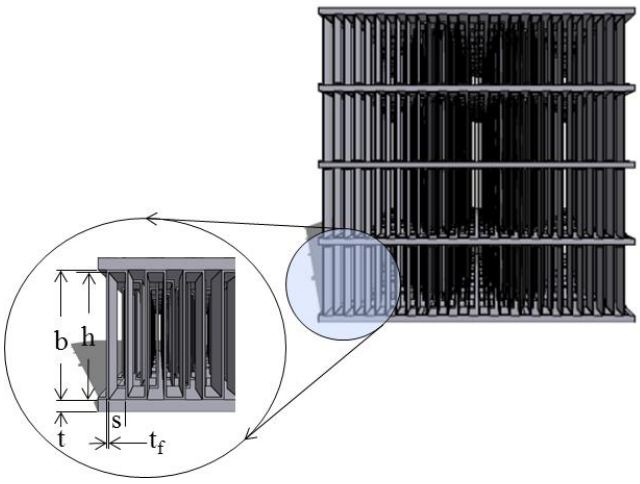

Figure 23: Schematic of typical counter flow compact heat exchanger.

2.6.1 Heat Exchanger Sizing Algorithm

The equations and parameters describing the physical geometry of a compact heat exchanger can be found in Table 2. The parameters describing the physical geometry, shown schematically in Figure 23, are shown to be related to five important characteristics of a compact heat exchanger. They are the hydraulic diameter, porosity, and the non-dimensional aspect ratios α, δ and γ.

Table 2: Equations describing the physical geometry of the new heat exchanger model[15].

Variable	Description	Model Equation
D_h	Hydraulic diameter (m)	$D_h = \frac{4shl}{2(sl + hl + t_f h) + t_f s}$
σ	Porosity	$\sigma = \frac{s(b - t_f)}{(s + t_f)(b + t)}$
β	Surface area density of one side of heat exchanger (m^2/m^3)	$\beta = \frac{4\sigma}{D_h}$
s	Fin channel width (m)	
h	Fin channel height (m)	
l	Fin strip length (m)	
b	Plate gap thickness (m)	
t_f	Fin thickness (m)	
t	Plate thickness (m)	
L	Overall heat exchanger length (m)	$\alpha = \frac{s}{h}, \quad \delta = \frac{t_f}{l}, \quad \gamma = \frac{t_f}{s}$
α	Non-dimensional aspect ratio	
δ	Non-dimensional aspect ratio	
γ	Non-dimensional aspect ratio	

The hydraulic diameter is related to the Reynold's number, which impacts not only the heat transfer capabilities of the heat exchanger, but the pressure drop across it. The porosity is one measure of how compact the heat exchanger is and is defined as the ratio of enclosed (wetted) volume to total volume. Another measure of compactness is the heat transfer surface area density, β, the ratio of wetted surface area to total volume. Typically, for an offset strip-fin (OSF) compact heat exchanger, β ranges from 300 to 3000 m^2/m^3. The non-dimensional aspect ratios defined in Table 2 are used in the correlations to determine f, the Fanning friction factor, and j, the Colburn coefficient. Both of which are defined in Table 3.

Table 3: Equations describing iterative process used to size heat exchanger[15].

Variable	Description	Model Equation
f	Fanning friction factor	$\mathrm{Re} = \frac{\rho u D_h}{\nu}$
j	Colburn coefficient	$f = 9.6243\,\mathrm{Re}^{-0.7422}\,\alpha^{-.01856}\delta^{0.3053}\gamma^{-0.2659}\left(1+7.669\times10^{-8}\,\mathrm{Re}^{4.429}\,\alpha^{0.92}\delta^{3.767}\gamma^{0.236}\right)^{0.1}$
ε	Heat exchanger effectiveness	$j = 0.6522\,\mathrm{Re}^{-0.5403}\,\alpha^{-0.1541}\delta^{-0.1409}\gamma^{-0.0678}\left(1+5.269\times10^{-5}\,\mathrm{Re}^{1.34}\,\alpha^{0.504}\delta^{0.46}\gamma^{-1.055}\right)^{0.1}$
$\dot{Q}$	Heat load (W)	$\varepsilon = \frac{Q}{Q_{\max}} = \frac{\dot{Q}}{\left(\dot{m}\times c_p\right)_{\min}\left(T_{1,i}-T_{2,i}\right)}$
$\dot{Q}_{\max}$	Design heat load (W)	
Ntu	Number of thermal units	$Ntu = \frac{\varepsilon}{1-\varepsilon}$
N	Ntu for one side	$N = \frac{2\times Ntu}{\eta_0}$
$A_{c,fluid}$	Fluid flow area	
Δp	Pressure drop (kPa)	$\Delta p = \frac{1}{2}\rho f\left(\frac{\dot{m}}{A_c}\right)^2\frac{4L}{D_h}$
G	Mass velocity $\left(kg/m^2\cdot s\right)$	$G_1 = \frac{\dot{m}_1}{A_{c,1}} = \sqrt{\frac{2\times\rho_1\times\Delta p_1\times j_1/f_1}{\mathrm{Pr}_1^{2/3}\,N}}$

2.6.2 Iterative Process to Solve for Area

An important aspect of the heat exchanger sizing algorithm is the iterative process used to size the heat exchanger, shown in Figure 24. Solving for area requires an iterative approach due to the implicit nature of the equations found in Table 3. Calculating the Reynold's number requires knowledge of u , the fluid flow velocity, which is a function of the volumetric flow rate and flow area. Of which volumetric flow rate is known, leaving flow area as the only unknown. Additionally, if area is assumed, working through the equations will yield the mass velocity term, G , which is a function of the mass flow rate and area. At this

point, it is possible to solve for the new flow area, however, unless the initial assumption for the flow area was correct, the flow area calculated will be different from the initial value. Thus, it is necessary to undergo the iterative process described below until the guess and output converge.

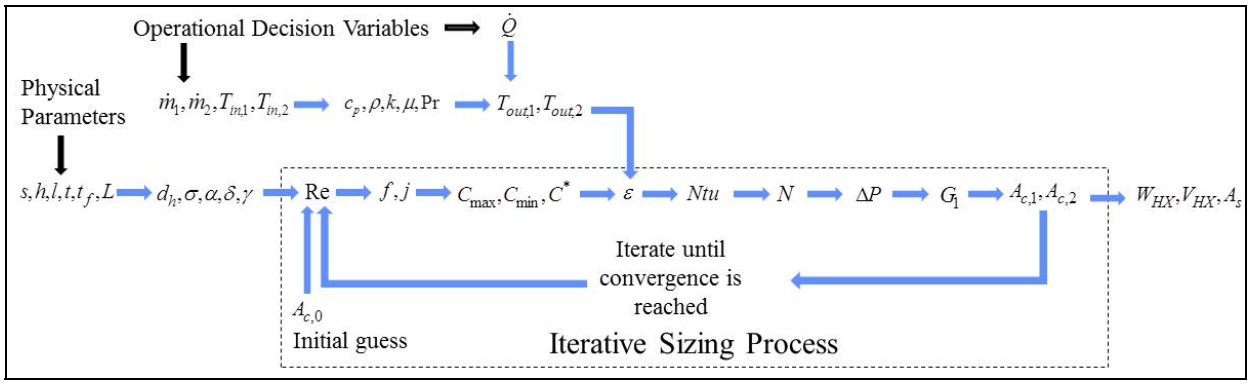

Figure 24: Iterative process used to size heat exchanger for each application.

Fast convergence will be guaranteed with a sufficiently close initial guess, however, this knowledge of both the operational and physical parameters. Global optimization techniques such as genetic algorithms (GA) or pattern search algorithms (PSA) eliminate some of the heuristic knowledge required to guarantee convergence.

Upon selection of these initial parametric values, the algorithm calculates the parameters required to begin the iterative process. The iterative process is displayed in Figure 24, with the correlating equations laid out in Table 3. This process was adapted from the equations presented by Hesselgreaves[15] and Kays & London.[16]

The terms f and j are unique in that they exhibit asymptotic behavior that negates the need for separate calculations for laminar, transitional, and turbulent flow regimes. Notice that these equations account for the geometry of the heat exchanger through the non-dimensional aspect ratios defined in Table 2. Additionally notice that the ε-NTU method was utilized to quantify the performance of the heat exchanger. The implementation of this method required several assumptions. The first assumption is that the fin efficiency was constant at 0.8. This assumption is valid for most heat transfer coefficients and fin materials used. Additional assumptions included constant properties (e.g. specific heat, density, viscosity), which are also valid for this application due to the relatively narrow temperature ranges that the system operates within.

Upon conclusion of the iterative process to determine flow area, the algorithm will output the final flow area. With this flow area, it is possible to determine the total weight and volume of the heat exchanger using the equations found in Table 4.

Table 4: Equations used to determine heat exchanger volume and weight[15].

Variable	Description	Model Equation
W_{hx}	Weight of heat exchanger (kg)	$W_{hx} = W_{s,1} + W_{s,2} = \rho_m L\left(\frac{A_{c,1}}{\sigma_1}(1-\sigma_1)+\frac{A_{c,2}}{\sigma_2}(1-\sigma_2)\right)+\left(A_{c,1}\rho_1 + A_{c,2}\rho_2\right)L$
W_s	Weight of one side of heat exchanger (kg)	
V_{hx}	Volume of heat exchanger (m^3)	$V_{hx} = L\left(\frac{A_{c,1}}{\sigma_1}(1-\sigma_1)+\frac{A_{c,2}}{\sigma_2}(1-\sigma_2)\right)$
A_s	Surface area of one side of heat exchanger (m^2)	$A_s = \beta\left(L\left(\frac{A_c}{\sigma}(1-\sigma)\right)+A_c\right)$

3.0 RESULTS

As a representative study, a generic modern long range strike aircraft was modeled over a 200 minute mission utilizing the models previously described with only shell and tube type heat exchangers. The intention of the mission profile, depicted in Figure 25, is to provide sufficient coverage of the flight envelope to demonstrate performance of the integrated model in each of the segments of interest: pre-flight ground hold, accelerate, climb, cruise, descent, low altitude flight, post-flight ground hold. The ambient conditions for the mission were as specified by the standards for a Mil-HDBK-310 10% Hot Day.

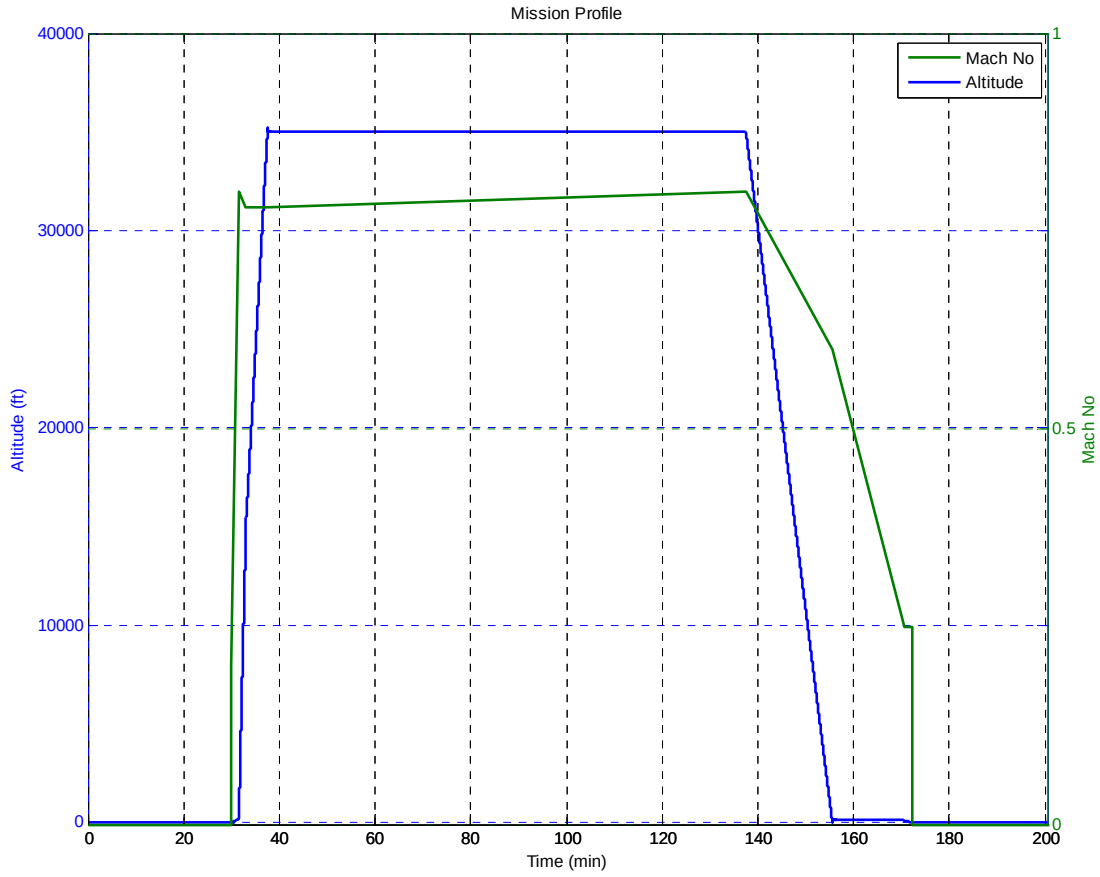

Figure 25: Mission profile - altitude and Mach number.

3.1 Trade Study Results

The objective of the trade study is to investigate the performance benefits associated with different PTMS architectures. The function of the PTMS is to cool the thermal loads on the aircraft and the performance of the PTMS can be assessed by the thermal margin and the required energy to refrigerate the loads. Improved PTMS performance will provide both an increased thermal margin, which would allow for increases in thermal loading or the extension of missions capabilities, and will also require less energy to refrigerate the aircraft loads.

One important measure for PTMS thermal margin is fuel tank temperature, which has a chosen maximum temperature limit of 138F. A metric for PTMS energy consumption is the fuel required to complete the mission with an improvement resulting in a reduction in fuel consumption. The performance associated with each PTMS is evaluated for fuel tank temperature as a function of mission time (Figure 27) as well as fuel weight as a function of mission time (Figure 26).

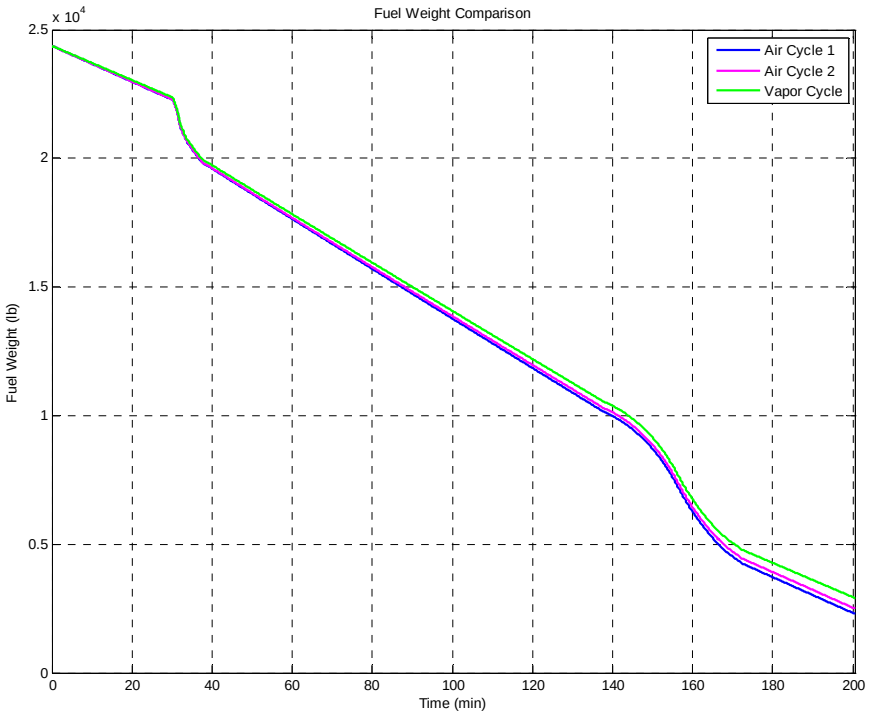

Figure 26: Total fuel burn comparison.

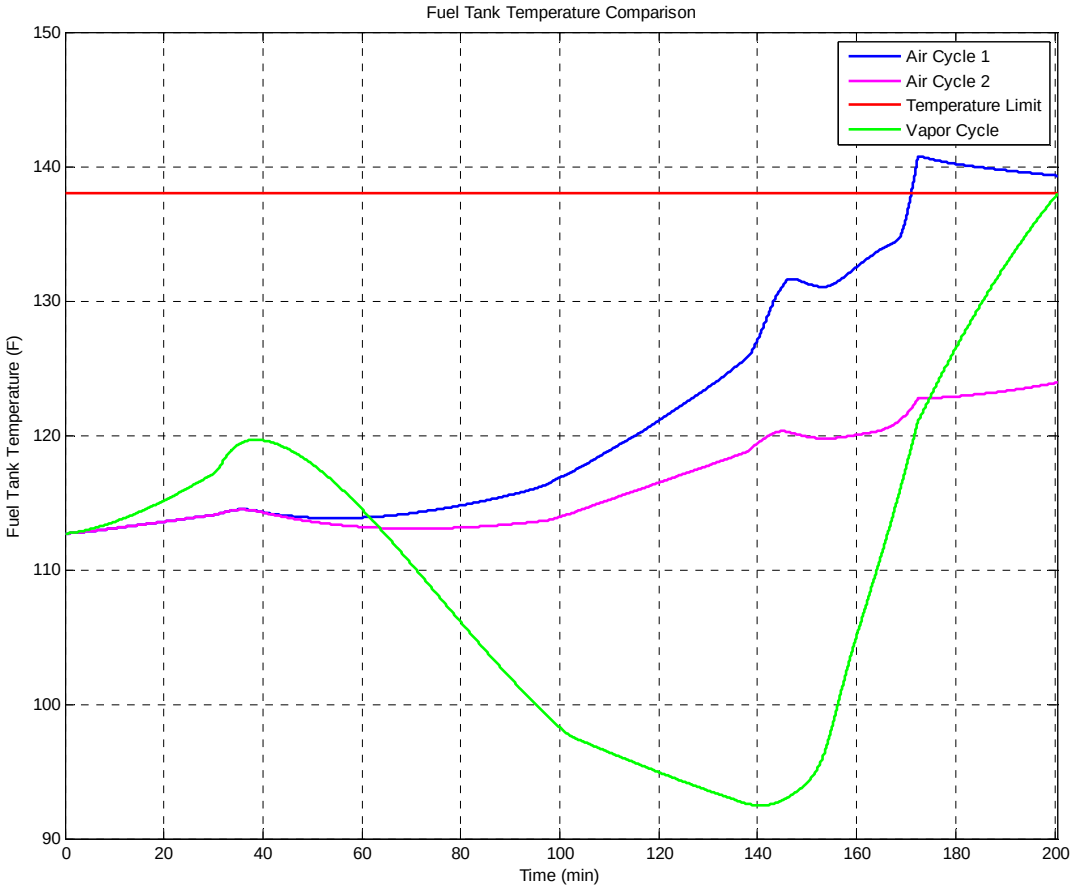

Figure 27: Fuel tank temperature comparison.

Figure 27 compares the fuel tank temperature of the three PTMS architectures over the mission. In air cycle architecture #1, the fuel tank thermal limit is exceeded after 170 minutes with a peak fuel tank temperature of 140F. The exceeded thermal limit would require alteration of the mission resulting in reduced mission capability. In air cycle architecture #2, the fuel tank thermal limit is not reached. The peak fuel tank temperature is 123F which results in a 17F increase in thermal margin as compared to air cycle architecture #1. Architecture #2 employs a lower temperature primary heat sink, main engine fan stage one in contrast to the second fan stage in architecture #1, which results in a reduced use of the secondary HLL heat sink. The HLL heat sink ultimately sinks heat to the fuel resulting in an increase in fuel temperature. The reduced use of the HLL heat sink results in a reduction in fuel tank temperatures. The peak fuel tank temperature of 137F is reached in the vapor cycle architecture. As in the second air cycle architecture, the fuel tank thermal limit is not reached.

Figure 26 compares the fuel consumed during the mission for the three PTMS architectures. Improved performance of air cycle architecture #2 results in a 205lb fuel savings compared to air cycle architecture #1. The lower temperature heat sink in architecture #2 results in lower power consumption compared to architecture #1. The vapor cycle architecture provides fuel savings compared to either of the two air cycle architectures: savings of 619 lb and 414 lb, respectively. The vapor cycle is powered from engine shaft

extraction which results in reduced bleed air extracted for the engine. The reduced extracted bleed air results in the reduced fuel consumption.

4.0 NEXT STEPS

The present effort represents a fundamental effort in modeling and integration of a system level thermal aircraft model. The ultimate goal is to validate both the component and integrated system models against data measured from real-time hardware-in-the-loop test facilities. In turn, validated system level models will allow meaningful optimization studies to be pursued. Toward realizing this goal, future work is planned along a number of fronts, including upgrading the fidelity of the present component models as well as expanding the scope of the analysis to include interactions with the actuation and electrical power systems. Specifically, the vapor cycle model requires additional dynamic modeling to handle transient effects. Next, there are plans to explore the design and performance of a hybrid PTMS system that would combine vapor cycle and air cycle subsystems in one system. It is believed that a complex trade space such as that for a hybrid PTMS design can be best explored with an integrated aircraft level simulation such as the one described here. Additional future work for mission level modeling includes plans for other aircraft platforms as well as for the inclusion of actuation and electrical power models. Also, a through process of verification, validation and certification will be accomplished. This will enable the determination of the uncertainty quantification of this type of analysis. Finally, more research needs to be accomplished with regards to subsystem control/interaction in the preliminary stages of vehicle design because this is a significant driver in TMS performance.

5.0 CONCLUSIONS

Thermal management is and will continue to be a first order forcing function in the preliminary design of advance aircraft whether commercial or military. A key aspect of TMS design is the effective integration of the various subsystems which are involved in the thermal system. The operation of these subsystems is transient in nature. The days of turning systems on for the duration of the flight without any changes to the operating conditions are over. “On-demand” system operation is needed to obtain the performance required of the aircraft. Because the engine is at the heart of the power/thermal system, the integration of the engine with the other subsystems of the vehicle is essential in designing an optimal TMS. The current state of the art regarding TMS modelling and simulation has been presented. Detailed discussions of the transient drivers of the engine, the fuel tanks and compact heat exchangers have been presented. The preliminary results from a tip-to-tail aircraft thermal model have been shown. The model includes an aircraft 6 degree of freedom model (6-DoF), a vehicle management system (VMS) model, an engine aerodynamic model, an engine thermal model, a vehicle thermal model (fuel tanks), a power thermal management system (PTMS) model, and various representative aircraft level heat loads. The model created has shown the capability to perform parametric studies that can be used as a basis for future optimizations.

6.0 ACKNOWLEDGEMENTS

The author gratefully acknowledges the support of the US Air Force Research Laboratory for sponsoring and funding this research. In addition, many individuals have contributed significantly to this research: at AFRL/RZP – Peter Lamm, Mike Corbett, Jon Zumberge, Steve Iden; at PCKA – Mark Bodie, Kevin McCarthy, Greg Russell, Eric Walters, Tim O’Connor, Eric Lucas; at Wright State University – Prof. Rory Roberts, Scott Eastbourn; at Virginia Polytechnic Institute – Prof. Michael vonSpakovsky, Peter Weise; at Georgia Institute of Technology – Adam Maser without their time and effort this manuscript would not be possible. It has been my pleasure to work with you all.

7.0 REFERENCES

[1] R. Simmons, "Design and Control of a Variable Geometry Turbofan with an Independently Modulated Third Stream," Ph.D. Dissertation, Aerospace Engineering Department, The Ohio State University, Columbus, Ohio, 2009.

[2] J. Lytle, "The Numerical Propulsion System Simulation: An Overview," *NASA/TM—2000-209915*, Cleveland, Ohio, June 2000.

[3] S. Jones, "An Introduction to Thermodynamic Performance Analysis of Aircraft Gas Turbine Engine Cycles Using the Numerical Propulsion System Simulation Code," *NASA/TM—2007-214690*, Cleveland, Ohio, March, 2007.

[4] M. Turner, J. Reed, R. Ryder, and J. Veres, "Multi-Fidelity Simulation of a Turbofan Engine With Results Zoomed Into Mini-Maps for a Zero-D Cycle Simulation," *NASA/TM—2004-213076*, Cleveland, Ohio, November 2004.

[5] J. Mattingly, W. Heiser, and D. Pratt, *Aircraft Engine Design*, Second Edition, AIAA Education Series, Reston, Virginia, 2002.

[6] P. Walsh and P. Fletcher, *Gas Turbine Performance*, Second Edition, Blackwell Science Ltd, Malden, Mass., 2004.

[7] "NPSS Humidity Addendum," NASA Glenn Research Center (NPSS/NICE), NPSS-User Rev: 1.6.5, March 2008.

[8] "NPSS Reynolds Addendum," NASA Glenn Research Center (NPSS/NICE), NPSS-User Rev: 1.6.5, March 2008.

[9] E. A. Thornton, Thermal Structures for Aerospace Applications, American Institute of Aeronautics and Astronautics, Inc., Reston, VA, 1996.

[10] E. K. P. Chong, S. H. Żak, An Introduction to Optimization, John Wiley and Sons, Inc. New York, NY, 2001.

[11] R. W. Truitt, Fundamentals of Aerodynamic Heating, The Ronald Press Company, New York, 1960.

[12] F. P. Incropera and D. P. DeWitt, Fundamentals of Heat and Mass Transfer, John Wiley and Sons, Inc., New York, NY, 2002.

[13] P. I. Cooper, "Absorption of Radiation in Solar Stills," Solar Energy, 12 (1969) 333-346.

[14] R. Siegel and J. Howell, Thermal Radiation Heat Transfer, Taylor and Francis, New York, NY, 2002.

[15] Hesselgreves, J. E. (2001). *Compact Heat Exchangers: Selection, Design and Operation* (1st ed.). Oxford: Elsevier. p. 179.

[16] Kays W. M., A. L. London, (1984). *Compact Heat Exchangers*, McGraw-Hill.